Upper lithospheric structure of the subduction zone offshore of southern Arauco peninsula, Chile, at ~38°S

Eduardo Contreras-Reyes,[1] Ingo Grevemeyer,[1] Ernst R. Flueh,[1] and Christian Reichert[2]

[1] A joint interpretation of swath bathymetric, seismic refraction, wide-angle reflection, and multichannel seismic data was used to derive a detailed tomographic image of the Nazca–South America subduction zone system offshore southern Arauco peninsula, Chile at ~38°S. Here, the trench basin is filled with up to 2.2 km of sediments, and the Mocha Fracture Zone (FZ) is obliquely subducting underneath the South American plate. The velocity model derived from the tomographic inversion consists of a ~7-km-thick oceanic crust and shows P wave velocities typical for mature fast spreading crust in the seaward section of the profile, with uppermost mantle velocities >8.4 km s^{-1}. In the trench–outer rise area, the top of incoming oceanic plate is pervasively fractured and likely hydrated as shown by extensional faults, horst-and-graben structures, and a reduction of both crustal and mantle velocities. These slow velocities are interpreted in terms of extensional bending-related faulting leading to fracturing and hydration in the upper part of the oceanic lithosphere. The incoming Mocha FZ coincides with an area of even slower velocities and thinning of the oceanic crust (10–15% thinning), suggesting that the incoming fracture zone may enhance the flux of chemically bound water into the subduction zone. Slow mantle velocities occur down to a maximum depth of 6–8 km into the upper mantle, where mantle temperatures are estimated to be 400–430°C. In the overriding plate, the tomographic model reveals two prominent velocity transition zones characterized by steep lateral velocity gradients, resulting in a seismic segmentation of the marine fore arc. The margin is composed of three main domains: (1) a ~20 km wide frontal prism below the continental slope with Vp ≤ 3.5 km s^{-1}, (2) a ~50 km area with Vp = 4.5–5.5 km s^{-1}, interpreted as a paleoaccretionary complex, and (3) the seaward edge of the Paleozoic continental framework with Vp ≥ 6.0 km s^{-1}. Frontal prism velocities are noticeably lower than those found in the northern erosional Chile margin, confirming recent accretionary processes in south central Chile.

Citation: Contreras-Reyes, E., I. Grevemeyer, E. R. Flueh, and C. Reichert (2008), Upper lithospheric structure of the subduction zone offshore of southern Arauco peninsula, Chile, at ~38°S, *J. Geophys. Res.*, *113*, B07303, doi:10.1029/2007JB005569.

1. Introduction

[2] Subduction at convergent margins has a major impact on both the incoming plate, which is forced to subduct, and the overriding block. As the incoming plate approaches the continent (or island arc), the lithosphere bends into the trench, producing a prominent bathymetric bulge, the outer rise. Depending on the age, rheology and stress state of the lithosphere, uplift may start several hundreds of kilometers from the trench axis. Plate bending, however, is strongest within 50 km of the trench, where bending stresses exceed the yield strength of the lithosphere, producing normal faulting [e.g., *Masson*, 1991; *Ranero et al.*, 2003; *Grevemeyer et al.*, 2005] and earthquake activity [e.g., *Chapple and Forsyth*, 1979; *Tilmann et al.*, 2008] seaward of the trench. Recent work suggested that bending-related faulting might be an evolutionary process, affecting structure and composition of the downgoing plate [*Ranero et al.*, 2003; *Grevemeyer et al.*, 2005, 2007]. At the trench, convergence between subducting and overriding plate causes either erosion of the upper plate typically when the sedimentary trench fill is <1 km and the convergence rate is >6.0 cm a^{-1} or accretion when the trench sediment thickness exceeds 1 km and convergence rate is <7.6 cm a^{-1} [*Clift and Vannucchi*, 2004]. Seismic data can be used to study the structure of incoming and overriding plate and reveal the interaction between both plates causing continents to grow or shrink as they collide in the trench.

[3] The southern central Chile margin hosted the rupture area of the great 1960 Chilean earthquake (M$_w$ ~ 9.5) [*Cifuentes*, 1989; *Barrientos and Ward*, 1990] and is characterized by a filled trench confined between two main

[1]Leibniz-Institute of Marine Sciences at the University of Kiel (IFM-GEOMAR), Kiel, Germany.
[2]Federal Institute for Geosciences and Natural Resources, Hannover, Germany.

oceanic features: the Juan Fernandez Ridge (JFR) and the Chile Rise (Figure 1). The southern central Chile margin was characterized by *Bangs and Cande* [1997] using structural constraints from multichannel seismic reflection data. Main features were a 15–20 km wide accretionary prism and a ~2 km thick trench fill. The backstop underlying the continental slope and its velocity structure, however, were poorly resolved. *Krawczyk et al.* [2006] used seismic refraction and wide-angle reflection data from an amphibious experiment to yield structural constraints of the entire subduction zone system offshore of the southern Arauco peninsula at ~38°S. Their final velocity-depth model concentrated on the nucleation area of the great 1960 earthquake more than 80 km landward of the trench and hence put less emphasis on the marine fore arc. To refine the crustal model of the accretionary complex, marine fore arc and downgoing plate, we reanalyzed a subset of the Subduction Process Off Chile (SPOC) data [*Krawczyk et al.*, 2006] and extended the profile across the trench–outer rise seaward of the trench to study the impact of bending-related faulting on the structure of the incoming plate. We integrated multichannel seismic reflection (MCS) data and seismic refraction and wide-angle reflection data into our inversion and performed a joint refraction and reflection traveltime tomography to obtain a detailed velocity model of the marine fore arc and the incoming/subducting oceanic lithosphere off Arauco peninsula, south central Chile (~38°S).

[4] One of the aim of this study is to investigate the evolution of the seismic structure of the incoming/subducting oceanic lithosphere. Prior to subduction the oceanic lithosphere suffers from plate bending, causing normal faulting [e.g., *Masson*, 1991; *Ranero et al.*, 2003] and earthquake activity ranging from microearthquakes of $M_w < 1$ [*Tilmann et al.*, 2008] to large intraplate earthquakes of $M_w > 6.5$ [e.g., *Chapple and Forsyth*, 1979; *Lefeldt and Grevemeyer*, 2008]. Bending-related faulting modifies the porosity structure and hydrogeology of the oceanic lithosphere and thus affects the subduction water cycle [*Ranero et al.*, 2003; *Grevemeyer et al.*, 2007]. A number of seismic experiments provided evidence that plate bending affects the subducting Nazca plate off northern [*Ranero and Sallares*, 2004], central [*Kopp et al.*, 2004], and southern central Chile [*Contreras-Reyes et al.*, 2007, 2008]. At the trench–outer rise area, the oceanic crust is pervasively fractured and hydrated by extensional bending-related faults, allowing the percolation of fluids to mantle depths and thus resulting in the weakening of the oceanic lithosphere prior to subduction [*Ranero et al.*, 2003]. During subduction, large intraplate earthquakes associated with normal faulting under the inner trench slope region suggest that plate bending and faulting continues until the plate unbends at greater depth [*Mikumo et al.*, 2002; *Vallée et al.*, 2003]. Thus oceanic lithosphere already hydrated and weakened at the outer rise is further fractured and faulted by extensional stresses underneath the overriding plate. *Ranero et al.* [2003] and *Ranero and Sallares* [2004] have suggested that the isotherm of 600°C (the depth limit of the brittle lithosphere) corresponds to a good proxy for the maximum depth of mantle hydration. However, this depth as a limit for lithospheric hydroalteration has not yet been constrained by active seismic studies. In this paper, we present new geophysical evidence for the evolution of the seismic structure of the oceanic Nazca plate prior to and during subduction, and
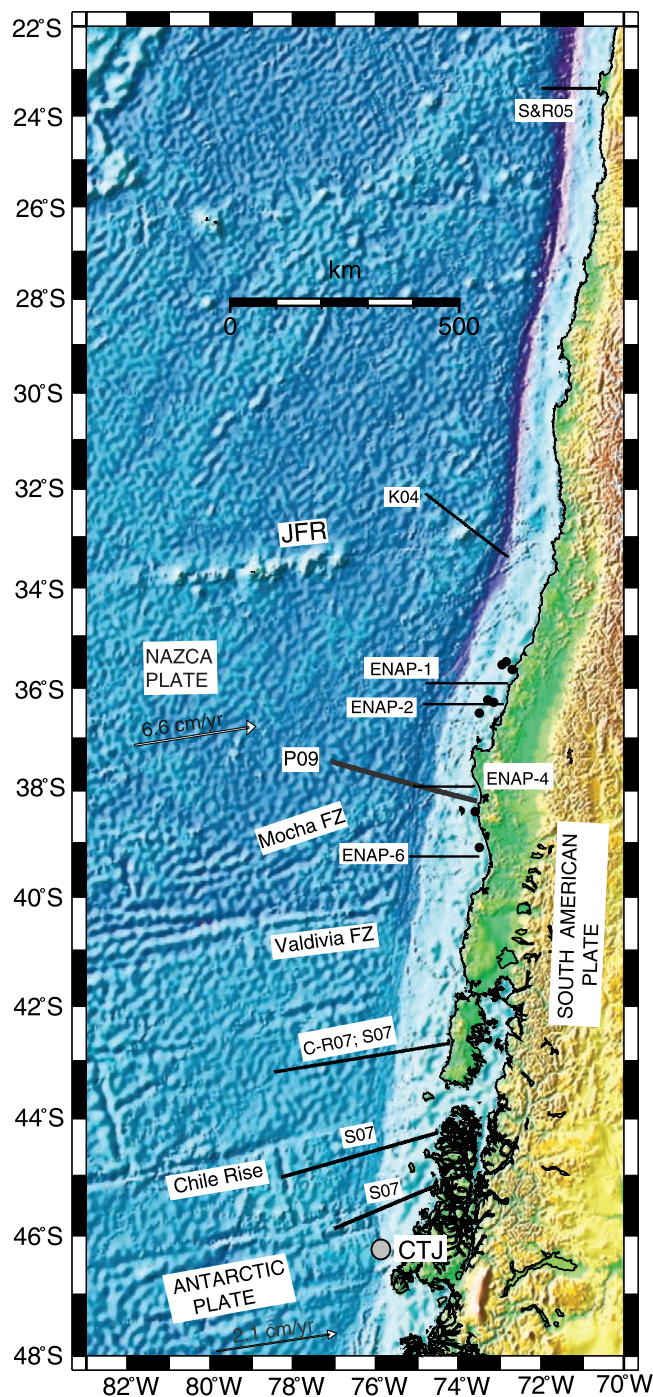

Figure 1. Geodynamic setting of Nazca, Antarctic, and South America plates; plates join at the Chile Triple Junction (CTJ), where the Chile Rise is currently subducting at ~46.4°S. The southern central Chilean margin is heavily sedimented and lies between the Juan Fernandez Ridge (JFR) and Chile Rise spreading center. P09 is the study profile (Figure 2). Small black dots indicate locations of the drilled wells [*Mordojovich*, 1974]. Seismic profiles ENAP-1, -2, -4, and -6 were studied by *Bangs and Cande* [1997] and *Diaz-Naveas* [1999], while black lines denote the published seismic profiles: S&R05 [*Sallares and Ranero*, 2005]; K04 [*Kopp et al.*, 2004]; C-R07 [*Contreras-Reyes et al.*, 2007]; and S07 [*Scherwath et al.*, 2007].

we assess the maximum depth of mantle alteration using wide-angle data.

[5] An additional aspect of this work is the seismic characterization of the continental margin off south central Chile. In this area, south of the JFR and north of the Chile Triple Junction the Chilean margin is characterized by accretion (Figure 1). Seismic data image up to 2.2 km of trench fill, resulting in an active frontal prism roughly 15–25 km wide [*Bangs and Cande*, 1997; *Diaz-Naveas*, 1999]. The proposed contact between the metamorphic/metasedimentary basement (continental backstop) and the young frontal prism is poorly imaged with seismic reflection data, and its crustal structure was mostly conceptual. A detailed tomographic seismic image of the upper plate derived from wide-angle data is presented in this paper for the first time. In addition, the erosional Chile margin to the north of the JFR consists of a frontal prism composed of slope debris and a middle slope prism of continental basement framework rock [*von Huene and Ranero*, 2003]. Its crustal structure has been investigated with multichannel reflection [*von Huene and Ranero*, 2003] and seismic refraction and wide-angle reflection data [*Sallares and Ranero*, 2005] and can be compared to the results from this study. We present new geophysical constraints for our understanding of erosion and accretion processes along the Chilean margin.

2. Geodynamic Setting

[6] The geological structure of the southern central Chile margin is controlled by the subduction of the oceanic Nazca plate beneath South America (Figure 1). The incoming Nazca plate subducts at ~6.6 cm a^{-1} with an azimuth of about N78°W [*Angermann et al.*, 1999]. The Chilean subduction zone is composed of two major segments defined by the incoming oceanic plate formed at two different spreading centers: north of the Valdivia Fracture Zone (FZ) the oceanic lithosphere was formed at the Pacific-Farallon spreading center more than 20 Ma ago [*Müller et al.*, 1997], whereas south of the Valdivia FZ it was created at the Chile Rise within the past 20 Ma [*Herron et al.*, 1981] (Figure 1). North of the Valdivia FZ, the seafloor spreading fabric of the Nazca plate strikes approximately 45° to the trench axis, whereas south of the Valdivia FZ it strikes ~15° to the trench axis. The Chile trench, Mocha and Valdivia FZs define a triangle called the Mocha block, which is an area of high stress concentration on the plate interface that acts as a boundary between two major segments of the Chilean subduction zone [*Barrientos and Ward*, 1990]. The main shock of the 1960 Chile earthquake (M$_w$ ~ 9.5), the largest ever instrumentally recorded, nucleated near the Mocha FZ and propagated southward for more than 900 km [*Cifuentes*, 1989; *Barrientos and Ward*, 1990].

[7] Our study area is located offshore southern Arauco peninsula, where the Mocha FZ trending N55°E, is currently entering the trench at ~38°S (Figure 2) and may be partly responsible for the uplift of the peninsula [e.g., *Kaizuka et al.*, 1973]. Because Mocha FZ strikes obliquely to the trench axis, the fracture zone intersection with the trench migrated southward at ~3.1 cm a^{-1} over the past million years relative to South America. North of the Mocha FZ, the plate age at the trench axis is ~30 Ma, whereas south of it the seafloor is about 24 Ma [*Tebbens et al.*, 1997]. The southern

central Chile trench is filled by terrigenous sediments sourced from the Andes [*Thornburg and Kulm*, 1987]. The deposited material is transported through submarine canyons and redistributed within the trench from south to north [*Thornburg et al.*, 1990; *Voelker et al.*, 2006].

[8] The primary geologic units exposed on land along the southern Chile coast are the continental basement rocks that are part of a Paleozoic accretionary complex and magmatic arc [*Mordojovich*, 1974; *Herve et al.*, 1988]. Exploratory drilling into the Arauco basin (see Figure 2 for location) reached metamorphic basement beneath ~500 m of Pliocene shelf sediments [*Mordojovich*, 1974]. Interpretation of seismic reflection data across the Arauco basin indicates that the oldest sediments in the depocenter of the fore-arc basin are Senonian [*Gonzalez*, 1989].

3. Characterization of Geological Structures From Seismic Reflection and Bathymetric Data

[9] Seismic reflection and swath bathymetric data were acquired offshore Arauco peninsula during the SPOC and TIPTEQ projects using R/V *Sonne* in 2000/2001 and 2004/2005, respectively [*Reichert et al.*, 2002; *Krawczyk and The SPOC Team*, 2003; *Flueh and Grevemeyer*, 2005; *Scherwath et al.*, 2006]. The seismic signals for the seismic reflection experiment were generated by a tuned set of 20 air guns with a total volume of 51.2 L. The multichannel seismic reflection data were analyzed using standard processing, including rebinning, normal move out correction, stacking, deconvolution, and poststack time migration. A predictive deconvolution with two gates, for the shallow sedimentary events and the deeper crustal events, was applied before the stack. A space and time variant frequency filter prior to a poststack migration completed the processing flow [*Reichert et al.*, 2002]. Seismic reflection data are displayed in Figures 3 and 4.

3.1. Trench–Outer Rise Area

[10] Seaward from the trench axis (>70 km) the oceanic plate is covered by a thin 0–400 m layer of pelagic sediments, which is draped by a much thinner and transparent blanket of hemipelagic mud. Here, high-resolution multibeam bathymetric mapping shows the SE-NW trending topographic pattern of the tectonic fabric formed at the spreading center, which is overprinted by horst-and-graben structures caused by bending-related faulting (Figure 2). Roughly 50 km off the trench axis, turbidites begin to fill the graben-like structure and overlay pelagic sediments, forming a sedimentary sequence with increasing thickness toward the trench (Figure 3). The trench fill wedge is ~40 km wide, with a maximum thickness of ~1900 m of turbidites overlying a ~300 m thick sequence of hemipelagic/pelagic sediments (Figure 3). Moho reflections occur at ~2.3 s below the top of the oceanic basement and can clearly be identified in the seismic section (Figure 3a).

[11] The Nazca plate carries seamount "chains" rising up to 2 km above the surrounding seafloor and elongated ridges aligned subparallel to the trend of the Mocha FZ (Figure 2). Approaching the trench, these edifices become progressively buried by sediments (Figure 2). The traverse ridge of the Mocha FZ is usually not higher than 700 m. At ~25 km seaward of the deformation front, a 5 km wide trench axial
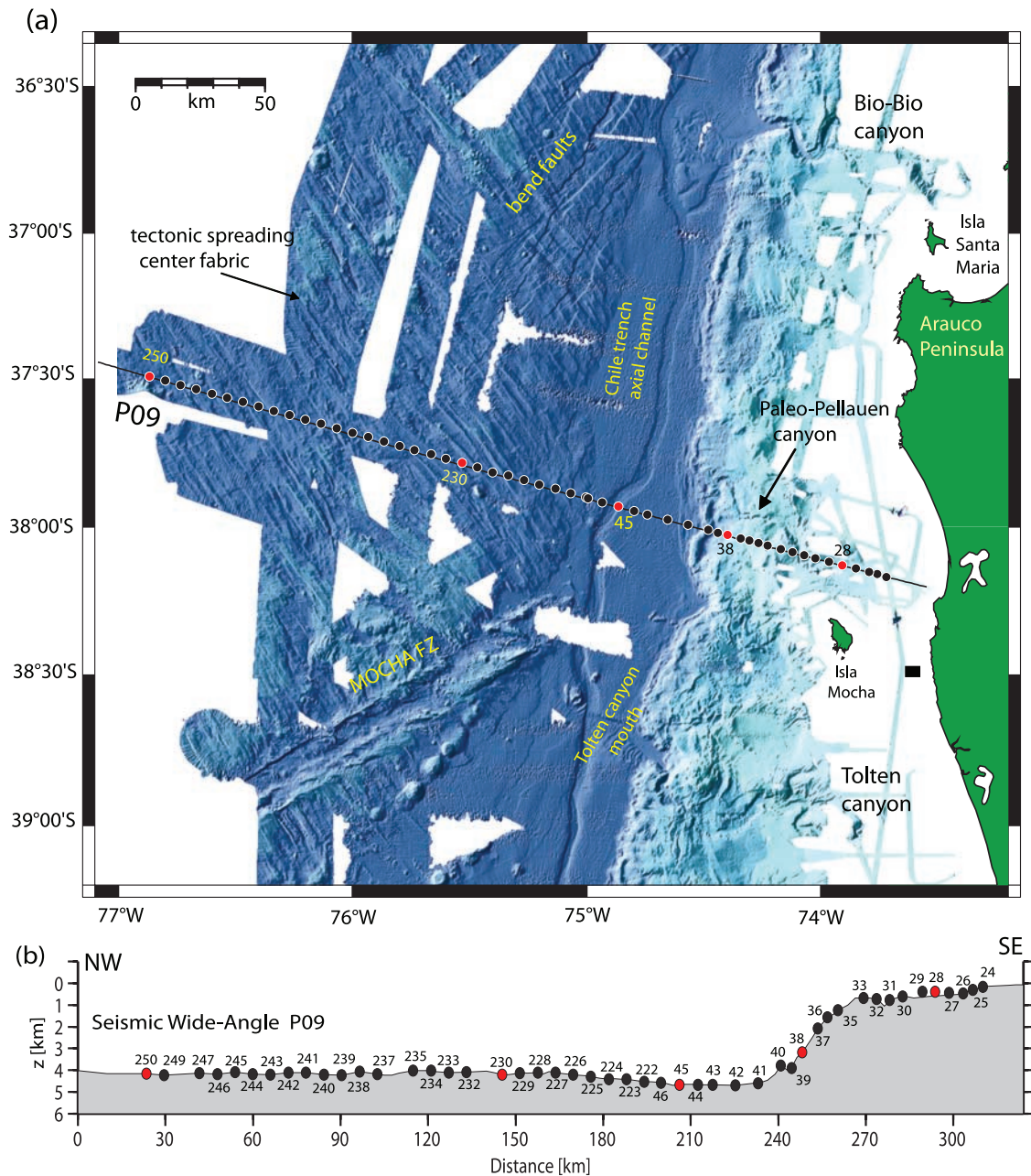
Figure 2. (a) High-resolution bathymetric image of the seafloor off Arauco peninsula. Solid black line is the integrated TIPTEQ and SPOC reflection and refraction profiles, while red dots and station numbers indicate the five stations (250, 230, 38, 45, 38, and 28) shown in Figure 5. Solid black rectangle denotes the location of the well drilled by ENAP [*Mordojovich*, 1974]. (b) Seismic profile P09 and numbers of the 48 OBH/S stations used in the traveltime tomographic inversion.

channel cuts into the seabed. The axial channel is buried by turbiditic deposits, and coincides with a horst-and-graben fault (Figure 3b). Toward the trench, bending-related faults tend to continue and cut often through the entire trench fill (Figure 3). In addition, the top of the oceanic crust becomes rougher in the trench–outer rise area, which might be caused by the combined effect of bending-related faulting and the rough relief of the Mocha FZ, which intersects the seismic line in the vicinity of the trench axis (Figure 2).

3.2. Frontal Accretionary Prism

[12] Seismic reflection data reveal a well-developed frontal thrust and current active off scraping of the trench fill (Figure 4c). A succession of small sedimentary ridges define the onset of the preaccretionary prism, which strikes parallel to the trench axis and coincides with a set of reverse faults imaged in the seismic reflection data (Figure 4). The thrust faults develop at depth, and some of them reach the seafloor crosscutting the entire trench fill sequence (Figure 4c). The largest accretionary ridge shown in Figure 4c marks the
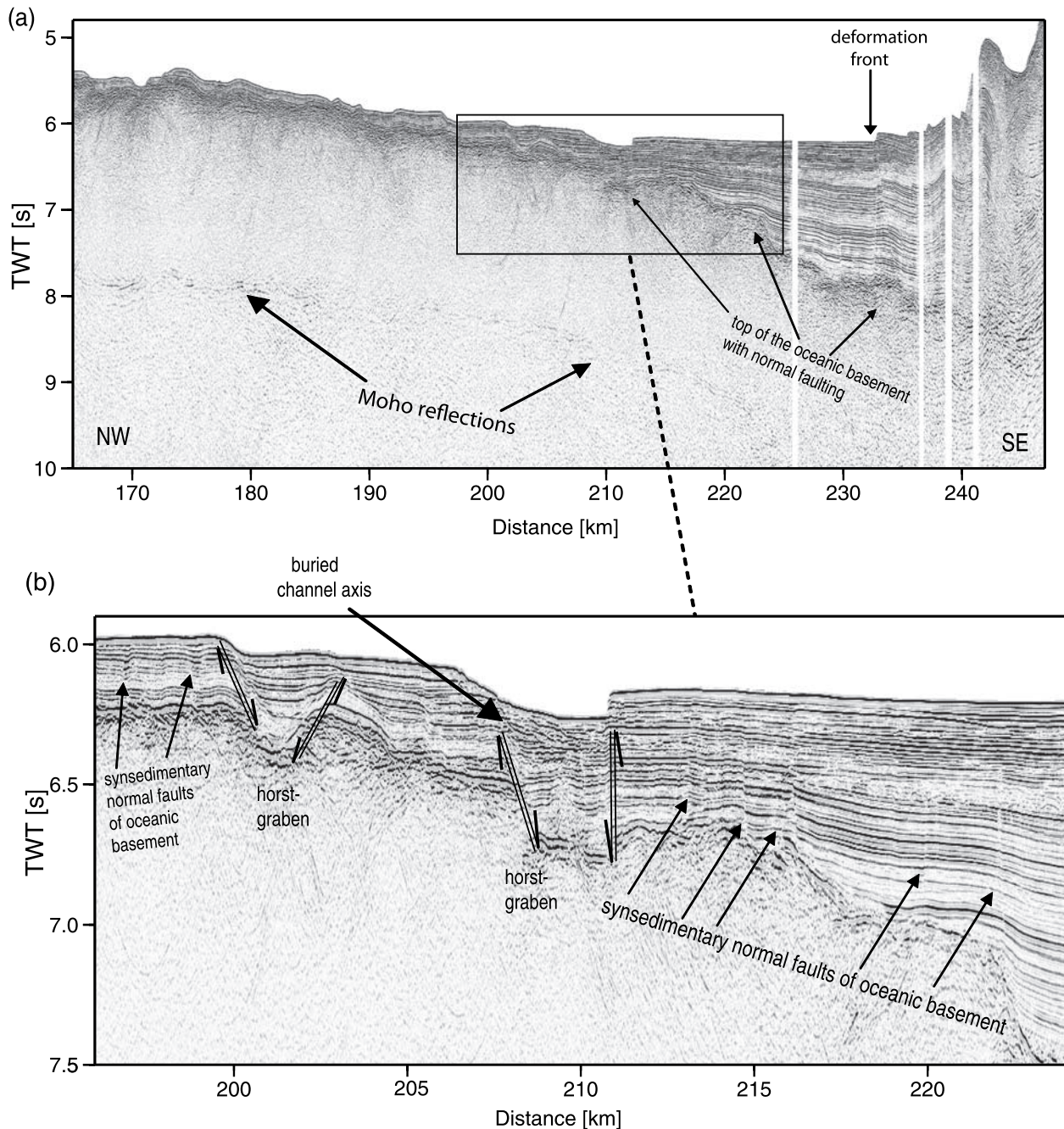
Figure 3. (a) Poststack time migration of the trench−outer rise and deformation front areas of seismic profile P09. (b) The seaward limit of the smooth trench is marked by the notably rough topography of the igneous basement. Its surface displays a characteristic, linear, topographic pattern caused by crustal horst-and-graben structures, masked by a thin sediment cover. The outer trench slope is disrupted by a set of subparallel normal faults that cut the oceanic crust.

onset of the lowermost slope, and its stratigraphy reveals compressional folding.

3.3. Fore-Arc Basin

[13] The Arauco fore-arc basin consists of a depression between the coastal Cordillera and the horst block of the basement filled with more than 3 km of late Cretaceous and Tertiary clastic sediments in the depocenter [*Gonzalez*, 1989]. From base to top, the shelf basin consists of (1) Senonian, (2) Paleocene-Eocene, (3) Oligocene-Miocene, and (4) Pliocene

to Quaternary clastics [*Gonzalez*, 1989]. The poststack time migration cross section shown in Figure 4a images the sedimentary Arauco basin just 20 km north of the Isla Mocha (Figure 2). Here, the depocenter of the basin lies 50 km landward of the deformation front with maximum sediment thickness of 1.7 s two-way time (TWT). Some inverted faults cutting the metasedimentary basement can be identified by offsets at the eastern part of the depocenter (Figure 4a). A striking feature at profile km ∼276 is the deep incision left by the path of the paleo-Pellahuen
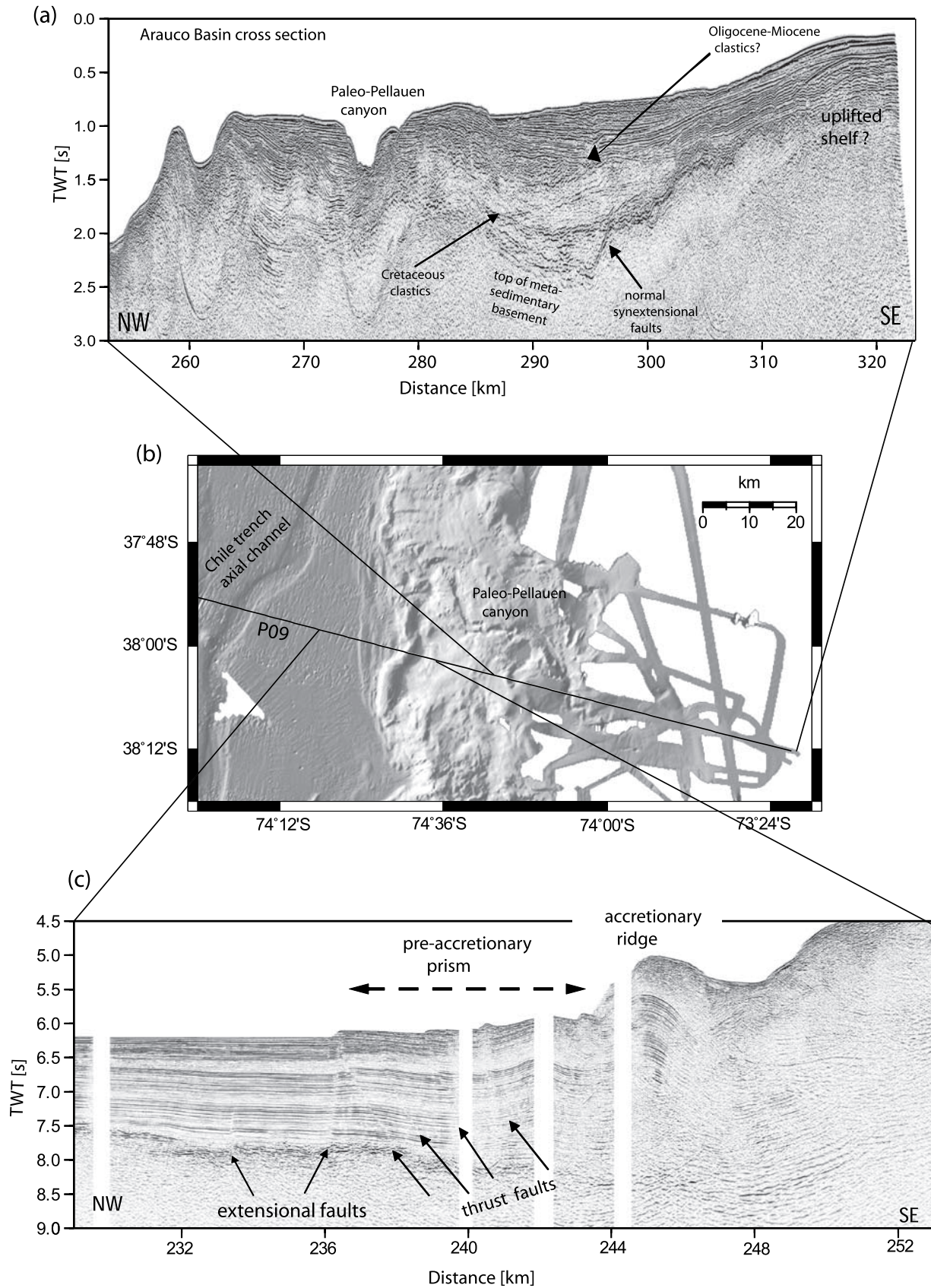
Figure 4. (a) Shelf section of seismic line P09. (c) Offsets in the sediment-trench stratigraphy indicate the existence of reverse faults cutting the entire sedimentary sequence and some hundred meters of the oceanic basement. (b) The expression of these processes at the seafloor surface corresponds to a set of accretionary ridges seen in the bathymetry and defines the frontal thrust surfaces.
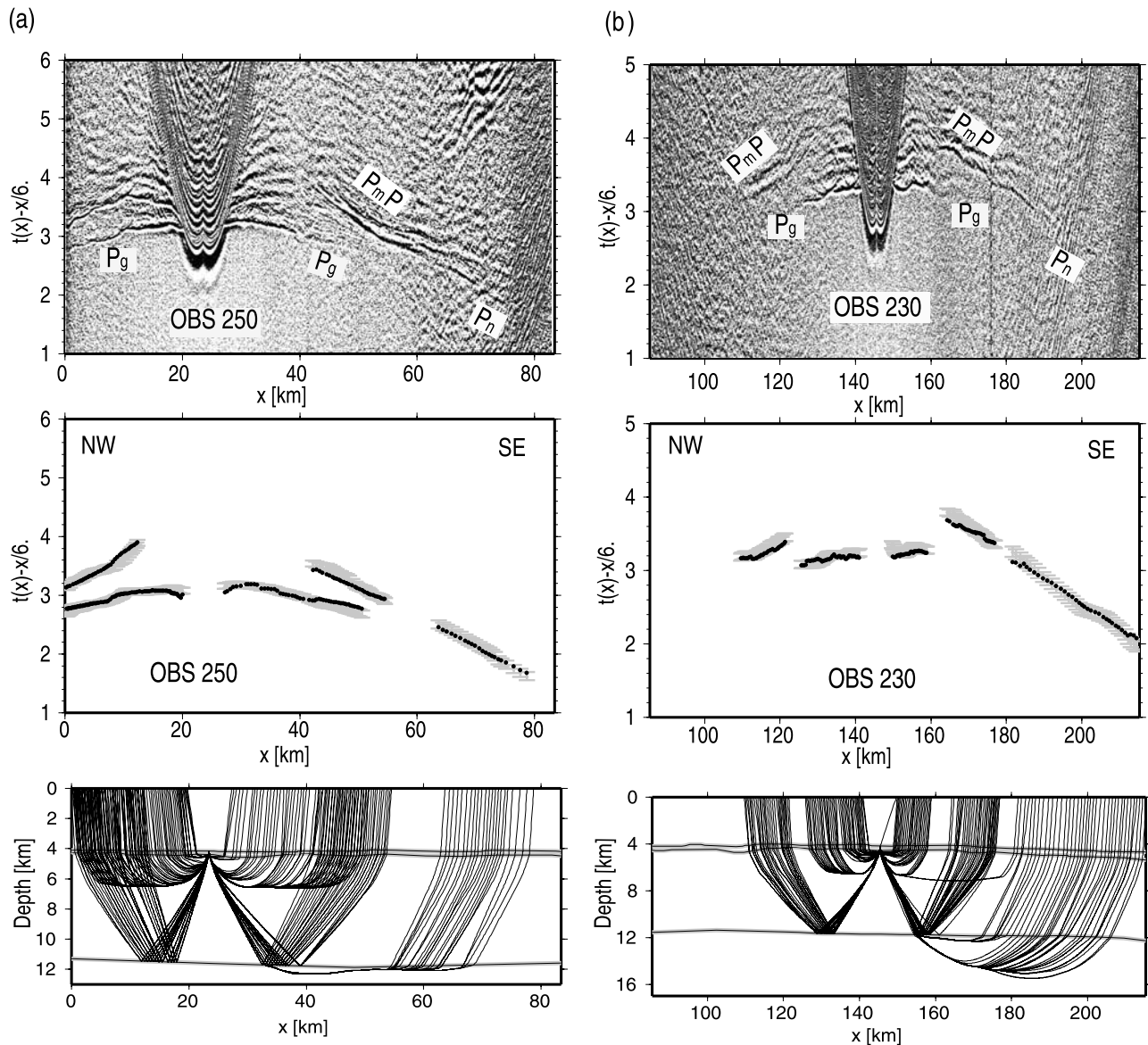
Figure 5. Examples of wide-angle seismic data with predicted travel times (black circles), which are computed based on the velocity model presented in Figure 6b. (a) OBH 250, (b) OBH 230, (c) OBH 45, (d) OBH 38, and (e) OBH 28.

submarine canyon. This is manifested by the deep erosion through all substrates, from unlithified shelf sediments to the metasedimentary basement. Another striking feature shown in Figure 4a is the uplifted shelf that belongs to the uplifted part of the Arauco peninsula [*Kaizuka et al.*, 1973; *Nelson and Manley*, 1992].

4. Wide-Angle Seismic Data

[14] Figure 2 shows the location of the seismic refraction/wide-angle reflection profile analyzed to study the incoming plate and marine fore arc at ∼38°S. The westernmost part of the line was obtained during the TIPTEQ cruise SO181 aboard R/V *Sonne* in 2005. Twenty-five seismic stations were placed along the ∼215 km long profile P09 [*Flueh and Grevemeyer*, 2005; *Scherwath et al.*, 2006]. This line extended SPOC profile P01 shot during SO161 in 2001

[*Krawczyk and The SPOC Team*, 2003] farther seaward across the trench–outer rise. Shots were recorded with a total number of 48 Ocean Bottom Seismometers (OBS) [*Bialas and Flueh*, 1999] and Ocean Bottom Hydrophones (OBH) [*Flueh and Bialas*, 1996], covering a distance of ∼250 km along the easternmost portion of the incoming oceanic Nazca plate, and ∼75 km along the westernmost portion of the continental margin (Figure 2). The seismic source for the refraction work carried out during TIPTEQ was a cluster of 8 × 8 L G guns, providing a total volume of 64 L for each shot. During SPOC a tuned array of 20 air guns provided a total volume of 51.2 L. Both sources were fired at a time interval of 60 s, which corresponds to an average shot spacing of ∼150 m. The record sections were interpreted after band-pass filtering (1 to 20 Hz) and predictive deconvolution. The signal-to-noise ratio obtained for most of the stations was high (Figure 5).
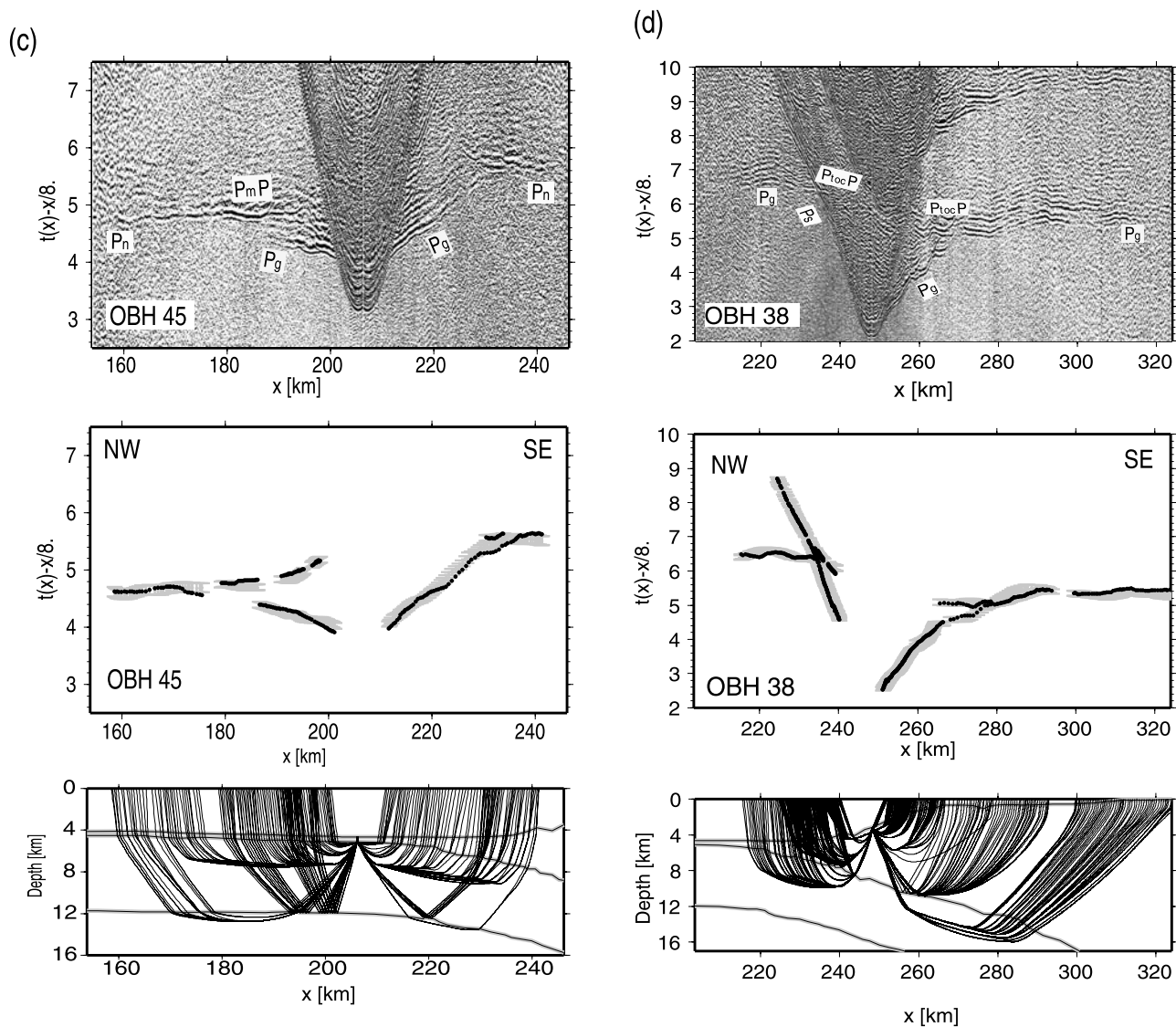
Figure 5. (continued)

[15] We have recorded crustal refractions (P_g), Moho wide-angle reflections (P_mP), upper mantle refractions (P_n), refractions through trench sediment (P_s), and reflections from the top of the oceanic crust ($P_{toc}P$) with excellent quality. Five examples of seismic record sections are shown in Figure 5, with their respective seismic phases identified. Apparent velocities influenced by the trench sediment and fore-arc structures decrease and increase landward, respectively. P_s and $P_{toc}P$ phases occur at approximately km 200 and hence 40 km from the trench axis. Figure 5d shows an example of record section OBH 38 positioned on the continental slope (see Figure 2 for location). The OBH data provide coverage of trench fill and accreted sediments down to basement at the NW and SE branch, respectively. Mantle, oceanic and continental crustal phases were recorded on most of the stations with excellent quality (Figures 5c–5e). Two striking features of the data set are: the rapid increase of apparent P_g velocities from profile km ~310, and the long offsets of P_n phases (>100 km) of some stations located on the continental shelf (Figure 5e).

[16] Picking of the seismic phases was done manually, and picking errors were assumed to be half a period of one arrival, to account for a possible systematic shift in the arrival identification, and were weighted according to the phase quality. Detailed information regarding average picking uncertainties and number of picks for the study profile are summarized in Table 1.

5. Traveltime Tomography Scheme

[17] We obtained the P wave velocity-depth structure using the joint refraction and reflection travel time inversion method of *Korenaga et al.* [2000]. This method allows joint inversion of seismic refraction and reflection travel time data for a 2-D velocity field. Travel times and raypaths are calculated using a hybrid ray-tracing scheme based on the graph method and the local ray-bending refinement [*van Avendonk et al.*, 1998]. Smoothing constraints using predefined correlation lengths and optimized damping constraints for the model parameters are employed to regularize an iterative linearized inversion [*Korenaga et al.*, 2000].
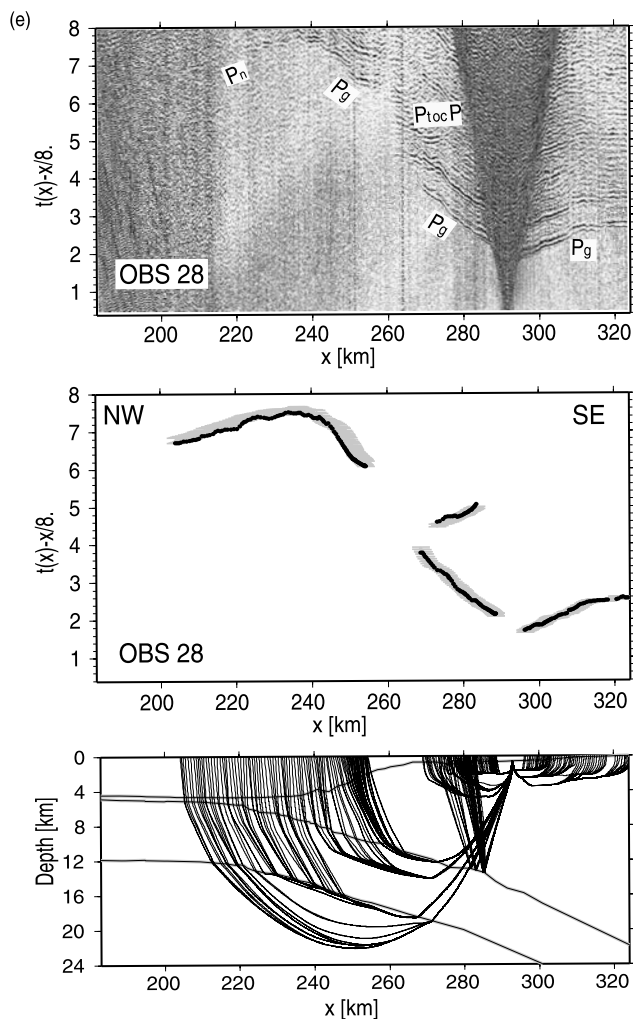
Figure 5. (continued)

of the sediments and the thickness of the sedimentary fore-arc basin, a combined approach using sedimentary refractions trough the basin and reflections from the top of the oceanic basement plus TWT reflection data was applied. Landward of roughly km 200, refracted P_s and P_g and reflected $P_{toc}P$ phases were used to directly invert for the velocity structure of the marine fore arc and geometry of the top of the oceanic plate. Inverted velocities and the depth of the plate boundary (igneous oceanic basement) were then held fixed in the following iterative inversions. The inner oceanic crust structure was inverted using P_g phases (first and later arrivals) to their maximum offset and P_mP phases in order to derive the velocity field and Moho depth. Similarly, the crustal velocities and Moho depth remained fixed for the next step of the inversion, where the upper mantle velocities were derived using oceanic P_n phases.

[19] The applied hybrid scheme uses both first and second arrivals to constrain the velocity model, without the need to disregard, for example, secondary arrivals such as lower crustal P_g phases, which become secondary arrivals where P_n arrivals overtake P_g. However, one problem of this approach is the identification and separation of crustal refractions P_g traveling through the continental and oceanic crust. This fact is critical in the landward portion of the model, where the small velocity contrast at the plate boundary makes it difficult to separate oceanic and continental P_g arrivals (Figure 5d). To solve this problem, we used for the upper plate inversion only P_g phases with offset up to 40 km (P_{g1}). For the lower plate and subsequent inversions, we decreased damping weight values in this area of the velocity-depth model and inverted P_g arrivals up to their maximum offsets (P_{g2}). Thus, arrivals at greater offset might constrain the upper structures. Several tests have shown that this approach fails at velocity discontinuities of high-velocity contrast (for example, Moho) but works adequately in continuous velocity boundary (landward part of the plate boundary). This is due to the fact that the tomographic inversion tends to smooth the lowermost and uppermost part of the upper and lower layer, respectively. As we described above, we use 2D velocity damping functions with either large or low weighting factors depending on the zone to retain or invert [Korenaga et al., 2000].

5.1. Reference Model and Inversion Parameters

[20] The 2-D velocity model is ~324 km long and 30 km deep. We used two floating reflectors to model (1) the interplate boundary beneath the continental margin and (2) the oceanic Moho. The initial geometry of the interplate

[18] The velocity model consists of the following geological units: (1) water, (2) sediments, (3) marine fore-arc basement, (4) oceanic crust, and (5) upper oceanic mantle. To derive the velocity depth model, the water depth was taken from the known bathymetry, which remained fixed during the inversion. Thickness of the sediment unit overlying the oceanic plate seaward of the trench wedge was obtained by picking and converting the vertical incidence reflections from the time migrated MCS data, using a constant velocity of 1.7 km s^{-1}. In order to obtain the velocity

Table 1. Summary of Traveltime Picks and Details of the Average Final Velocity Depth Model Shown in Figure 6b[a]

Phase	ΔT_{avg} (ms)	Reference Model T_{RMS} (ms)	Reference Model χ^2	Average Final Model T_{RMS} (ms)	Average Final Model χ^2
$P_{g1} + P_s$	55	222.36	15.5	52.79	0.85
$P_{toc}P$	70	198.70	9.52	75.00	1.24
P_{g2}	60	68.32	1.12	54.45	0.68
P_mP	75	99.70	2.02	76.91	1.20
P_n	75	135.75	3.93	75.54	1.17

[a]P_{g1}, continental crustal refraction or crustal refractions with offsets ≤40 km; P_s, trench fill refractions; $P_{toc}P$, reflection from the top of the oceanic crust; P_{g2}, oceanic crustal refraction or crustal refractions with offsets >40 km; P_mP, Moho reflections; P_n, oceanic mantle refractions; T_{RMS}, root-mean-square travel time misfit; ΔT_{avg}, average traveltime uncertainty; and χ^2, chi-square parameter.
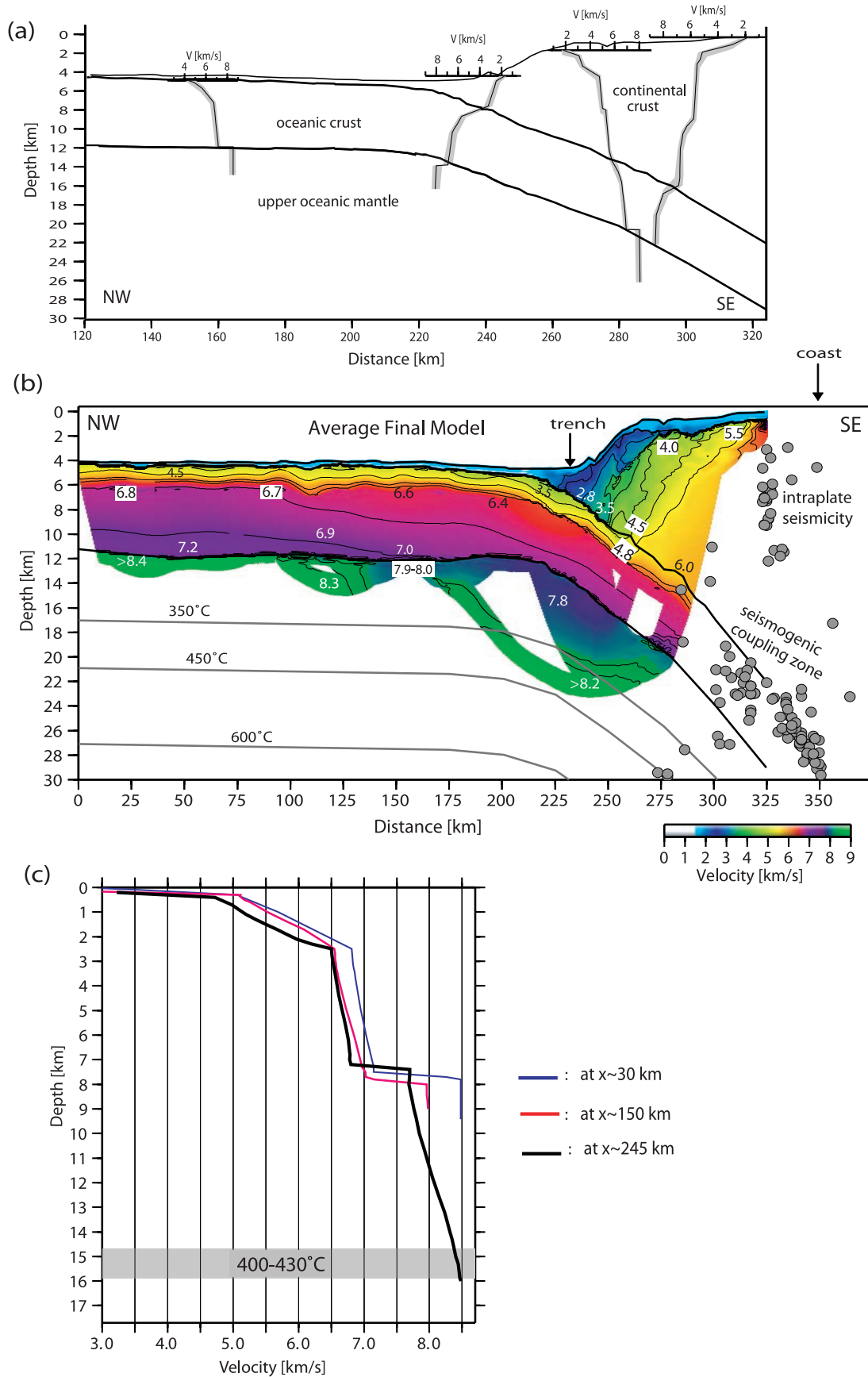
Figure 6

boundary reflector was obtained by forward modeling of the P_g, P_s and $P_{toc}P$ phases landward of profile km 200. Unfortunately, $P_{toc}P$ reflections landward of km 280 are weak and modeling of the reflector is difficult. We have therefore continued the geometry of the plate boundary toward the land by fitting it to hypocenter data of a temporary network in the Arauco peninsula which imaged the plate contact [*Haberland et al.*, 2006]. We prepared the reference model for the tomographic inversion by 1-D modeling of four OBH/S stations, which we consider as a key to define the general structure of the margin (E. Vera, personal communication, 2007). Figure 6a shows the locations of the four selected stations and their respective 1-D models. The 2-D seismic velocities of the reference model are calculated by linearly interpolating the velocities of the four 1-D velocity models. A similar approach is presented by *Sallares and Ranero* [2005].

[21] The root mean square travel time residuals (TRMS) obtained with the 2-D reference model are presented in Table 1. The horizontal grid spacing of the model used for the velocity inversion is 0.5 km, whereas the vertical grid spacing is varied from 0.1 km at the top of the model to 1 km at the bottom. Depth nodes defining the plate boundary and Moho reflectors are spaced at 1 and 2 km, respectively. We used horizontal correlation lengths ranging from 2 km at the top to 10 km at the bottom of the model, and vertical correlation lengths varying from 0.1 km at the top to 2.5 km at the bottom. Different tests showed that varying the values of correlations lengths by 50% does not significantly affect the solution. Because of the trade-off between correlation lengths and smoothing weights, we tried to use shorter correlation lengths and larger smoothing weights in order to reduce memory requirements [*Korenaga et al.*, 2000]. Depth and velocity nodes are equally weighted in the refraction and reflection travel time inversions.

5.2. Final and Uncertainty Velocity Models

[22] Tests with several starting models converge to nearly the same final model. In order to study the accuracy of the final model, we employed the Monte Carlo method [*Korenaga et al.*, 2000]. The uncertainty of a nonlinear inversion can be expressed in terms of the posterior model covariance matrix [e.g., *Tarantola*, 1987], which can be approximated by the standard deviation of a large number of Monte Carlo realizations assuming that all the realizations have the same probability [e.g., *Tarantola*, 1987]. The uncertainty estimated by this method should be interpreted as the uncertainty for our model parameters (i.e., starting velocity model and smoothing constraints). The procedure to estimate velocity-depth uncertainties consisted of randomly perturbing velocities and reflector depths of our reference model (Figure 6a). We generated 100 random

initial velocity models by adding randomly distributed smooth perturbations. The 2-D starting velocity models were obtained by linearly interpolating 1-D velocity profiles shown in Figure 6a, where gray areas represent possible variations in velocity randomization. The initial geometry of the interplate and Moho reflectors were randomly varied within a range of ±1.5 and ±2 km, respectively. In addition to the perturbed reference models we produced 100 so-called noisy arrival time sets constructed by adding random phase errors (±50 ms) and common receiver errors (±50 ms) to the original data set [*Korenaga et al.*, 2000]. Then we performed a tomographic inversion for each velocity model with one noisy data set, in order to estimate not only the dependence of the solution on the reference model but also the effect of phase arrival time picking errors. The mean deviation of all realizations of such an ensemble is considered to be a statistical measure of the model parameter uncertainties [e.g., *Tarantola*, 1987]. The stopping criterion for each inversion was $\chi^2 \sim 1$. Figure 6b shows the average velocity-depth model from the 100 final models, and detailed information regarding root-mean-square travel time misfits T_{RMS} and χ^2 parameters for the final average model is summarized in Table 1.

[23] The standard deviation of the calculated velocities (σ_v) is well constrained in the seaward portion of the velocity model (Figure 7). Landward from profile km 260, σ_v values in the upper plate increase to larger than 0.15 km s^{-1} due to the reduced data coverage (Figure 7a). Below the upper plate and within the upper oceanic crust, σ_v values increase up to 0.5 km s^{-1}, which indicates that velocities in this part of the model are largely unconstrained. The depth uncertainties of the interplate reflector oceanward from km~255 are lower than 0.1 km and reach 0.4 km at the landward edge of the velocity-depth model (Figure 7b), which is a zone characterized by the absence of $P_{toc}P$ reflections. Moho depth uncertainties seaward of km~270 range between 0.1 km and 0.3 km, and reach values higher than 0.5 km at the southeastern edge of the velocity model (Figure 7d).

5.3. Resolution Test

[24] To check the resolvability of the obtained velocity model we have created a synthetic model consisting of sinusoidal anomalies located both in the upper plate and the oceanic crust (Figures 8a and 8c). The anomalies are superimposed onto the final average velocity model shown in Figure 6b. The maximum amplitude of each anomaly is ±8% for the upper plate and ±6% for the oceanic crust (Figure 7). Synthetic travel time data with the same source-receiver geometry as in the real data set have been generated with the perturbed model, and they were inverted using an initial unperturbed model to see how well given pertur-

Figure 6. (a) One-dimensional reference models. (b) Final velocity-depth model derived by averaging all Monte Carlo ensembles, displayed together with projected earthquakes. The onset of shallow and coastal seismicity coincides roughly with the location of the most landward velocity transition zone inferred by our tomographic model. Hypocenters are taken from the TIPTEQ temporary seismological network [*Haberland et al.*, 2006]. Isotherm computations are based on the cooling of a semi-infinite half-space model [*Turcotte and Schubert*, 1982]. (c) One-dimensional velocity depth profiles are extracted from Figure 6b below sediments in order to compare the seismic structure of the "normal" (blue), altered incoming (red) and altered subducting oceanic lithosphere (black).
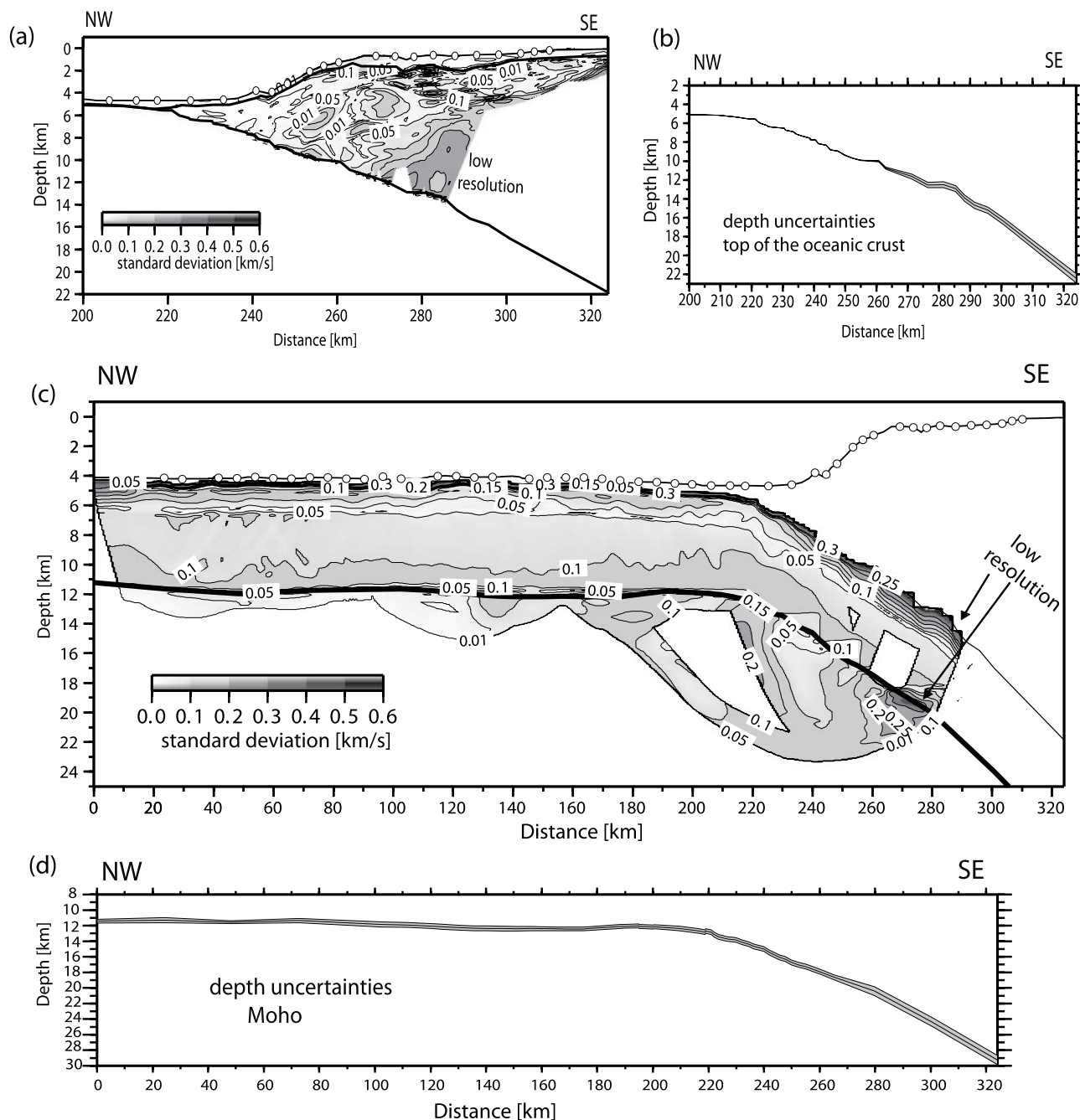
Figure 7. Velocity uncertainties for the (a) upper and (c) lower plates, and depth uncertainties for the (b) interplate and (d) Moho reflectors are shown.

bations are recovered. The recovery models are plotted in Figures 8b and 8d, which were gained after 5 and 3 iterations, respectively. The results show that most of the anomalies are reasonably well reproduced in position, shape and amplitude, except for two regions: (1) at the bottom of the upper plate at km~285 and (2) in the upper oceanic crust at km~250 (Figures 8b and 8d). These regions have low ray coverage and are poorly constrained, as is shown by the velocity uncertainty model (Figure 7). The recovered velocity anomalies in the upper part of the overriding plate, trench fill and oceanic crust seaward from km 220 show certain shape deterioration (Figure 7). Nevertheless, the results indicate that the geometry and instrument spacing

yields a sufficiently high resolution for these structural anomalies, discerning between positive and negative variations along the overriding plate and oceanic crust.

6. Results and Discussion

6.1. Evolution of the Seismic Structure of the Oceanic Lithosphere

6.1.1. Alteration of the Oceanic Crust

[25] In the seaward section of the tomographic model, the velocity structure of the oceanic crust provides uppermost and lowermost crustal velocities of ~4.4 and ~7.2 km s^{-1}, respectively. These velocities are typical for mature oceanic
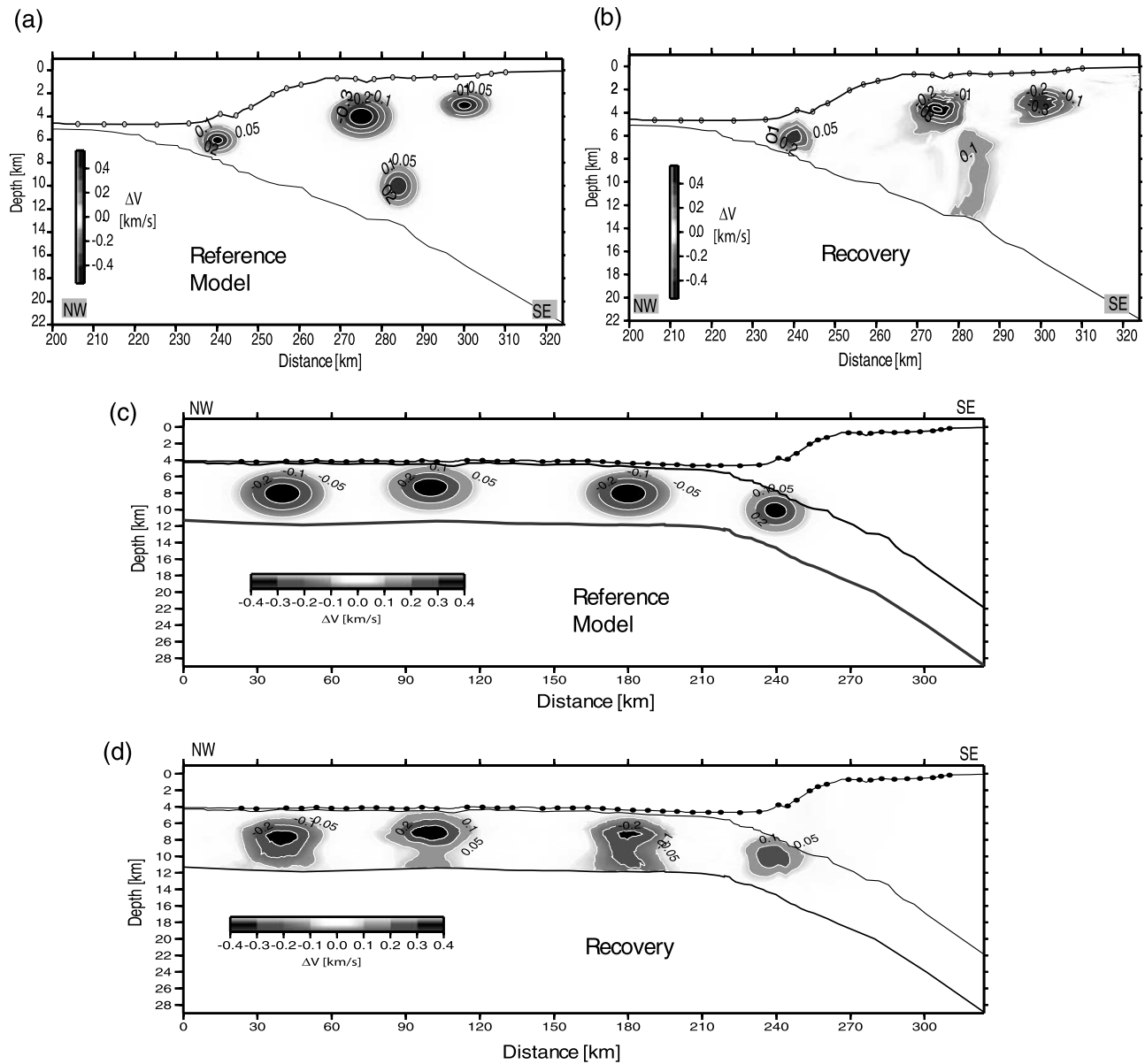
Figure 8. Results of resolution test. (a) and (c) Synthetic reference velocity models, consisting of four single sinusoidal anomalies superimposed onto the final velocity model shown in Figure 6b. (b) and (d) Recovery obtained after five and three iterations, respectively.

crust sufficiently far way from the ridge crests so that strong hydrothermal circulation has largely ceased [*Grevemeyer et al.*, 1999; *Grevemeyer and Weigel*, 1996]. The "typical" lower crustal velocities seaward of the trench–outer rise area are consistent with a undeformed and dry oceanic crust [*Carlson and Miller*, 2004; *Contreras-Reyes et al.*, 2007], which reflect an unaltered state of the crust away from the influence of tectonic extensional stresses in the outer rise region.

[26] Approaching the trench, however, velocities for the igneous crust begin to decrease 100–120 km seaward from the deformation front at crustal and uppermost mantle depths (Figure 6c). The uppermost crustal velocities decrease to values lower than 3.5 km s^{-1}, which are much less than typical uppermost velocities of layer 2 of mature oceanic crust (>4.5 km s^{-1}) [e.g., *Grevemeyer and Weigel*, 1996].

Low crustal velocities (<7 km s^{-1}) in the trench–outer rise area suggest a significant alteration of the porosity structure of the entire oceanic crust. The decrease of velocities is accompanied by an increase in the degree of fracturing (Figure 3), and probably coincides with activation of new cracks and normal extensional faults induced by bending-related faulting [*Ranero and Sallares*, 2004]. A similar trend in velocity reduction in the trench–outer rise area has been observed offshore Antofagasta at ~23.5°S [*Ranero and Sallares*, 2004], and offshore Isla de Chiloe at ~43°S [*Contreras-Reyes et al.*, 2007].

6.1.2. Alteration of the Oceanic Mantle Prior to Subduction

[27] Seaward of the trench, mantle velocities faster than 8.4 km s^{-1} are interpreted to be features of dry mantle peridotite [*Christensen*, 1996], indicating that the oceanic

Nazca plate approaches the subduction zone with an undeformed and dry mantle. Closer to the trench, however, mantle velocities decrease to minimum values of $\sim$7.8 km s^{-1} (Figure 6c), which is significantly lower than the velocity of mantle peridotite ($<$8.1 km s^{-1}). The velocity reduction suggests fracturing and/or hydration of the oceanic mantle in the trench–outer rise area. With an increasing degree of hydration and hence serpentinization the seismic compressional wave velocity is reduced from $<$8.1–8.3 km s^{-1} for pristine peridotite to $\sim$4.5 km s^{-1} at 100% transformation of peridotite to serpentinite [*Christensen*, 1996]. Perhaps, though, the ''normal'' uppermost mantle velocity $<$8.1 km s^{-1} between km$\sim$260 and km$\sim$280 is not a real feature but rather an artifact of the seismic tomography due to the low resolution, as indicated by the uncertainty of the velocity model (Figure 7c).

[28] Along seismic line Empresa Nacional del Petróleo (ENAP) 2 (Figure 1), *Diaz-Naveas* [1999] imaged bend faults cutting through the crust/mantle boundary into uppermost mantle. Similarly, to the south along seismic transect ENAP-6, *Diaz-Naveas* [1999] and *Grevemeyer et al.* [2005] imaged outer rise bending-related faults cutting at least $\sim$6 km into the uppermost mantle. Offshore Isla de Chiloe (at $\sim$43°S), a similar trend of P_n velocity reduction and relative high Poisson's ratios were observed [*Contreras-Reyes et al.*, 2007, 2008]. These observations give a clear sign of pervasive fracturing of the entire oceanic crust offshore south central Chile. Since water is required to alter mantle peridotite to serpentinite, pervasive fracturing of the entire crust is suggested for the lithosphere entering the subduction zone. Similar features have also been observed in central America [*Grevemeyer et al.*, 2007; *Ivandic et al.*, 2008], suggesting that serpentinization occurring in the trench–outer rise might be a characteristic feature of subduction.

6.1.3. Hydroalteration Processes Affecting the Subducting Oceanic Lithosphere

[29] Figure 6c summarizes the evolution of the seismic structure of the oceanic lithosphere as it approaches to the subduction zone. The velocity structure within the uppermost 8–10 km of the mantle imaged below the continental slope (Figure 6c) is characterized by a single velocity gradient of 0.1 s^{-1}. ''Normal'' mantle velocities of $\sim$8.4 km s^{-1} are reached roughly 6–8 km below the Moho. One mechanism to cause a vertical velocity gradient is impact of overburden pressure conditions at greater depth. *Christensen* [1996] used laboratory measurements to show that compressional velocities for serpentine at 200 MPa (typical pressure at the Moho) is about 0.1 km s^{-1} slower than serpentine at $\sim$400 MPa (estimated pressure at $\sim$16 km depth from the top of the lithosphere). Thus the steep gradient in the uppermost mantle could not be caused by lithostatic pressure alone. We favor the interpretation that a decrease in degree of hydration and fracture porosity may control the rapid increase in seismic velocities with depth. Mantle velocities of 8.4 km s^{-1} occurring at 16 km depth may define the lower limit of hydroalteration within the oceanic lithosphere, and thus may indicate the depth limit where seawater can penetrate. *Ranero et al.* [2003, 2005] and *Ranero and Sallares* [2004] have already suggested a depth limit of $\sim$20 km, which is based on the thickness of the brittle layer defined by the isotherm of 600°C. However, we calculated the geotherm for 30 Ma old

lithosphere [e.g., *Turcotte and Schubert*, 1982] and overlie the temperature model with the seismic tomographic model, which indicates that the 400–430°C isotherm matches the lower limit of hydroalteration of the oceanic mantle (assuming that the base of ''alteration front'' lies where upper mantle velocities reach values of $\sim$8.4 km s^{-1}) (Figure 6c). Thus the suggested isotherm of 600°C overestimates the amount of water carried with the incoming lithosphere into the deep subduction zone (Figure 6b).

[30] The transition from a tensional fault to a compressional fault may have important implications for percolation of water along the faults. While a tensional crack may support migration of water into the mantle, a compressional fault may prevent effective transfer of water into the mantle. Therefore, the maximum depth down to which water could penetrate would be at the neutral surface between extensional and compressional stresses, or rather slightly above the neutral surface, where bending stresses are too low to induce fracture and thus brittle faulting and hydroalteration. Estimating the location of the neutral plane between the compressional and tensional regime is difficult and depends on the rheology, thermal age and stress state of the plate. On the basis of statistical data, *Seno and Yamanaka* [1996] proposed that the 450°C isotherm is a good proxy for the depth limit between the tensional and compressional setting in the trench–outer rise area. The good match between the 400–430°C isotherm with the base of the alteration zone (8.3–8.4 km s^{-1} isoline) supports the idea that percolation of seawater might indeed be governed by tensional stresses, suggesting that the vicinity of the neutral plane where the tensional regime changes into a compressional regime defines the lower limit of mantle serpentinization.

6.1.4. Role of the Mocha FZ

[31] Alteration of the seismic structure of the oceanic crust may not only be induced by bending-related faulting, but also by the influence of the Mocha FZ which intersects the seismic line at the trench–outer rise area (Figure 2). Seismic tomography studies across the Clipperton transform fault revealed anomalously low velocities of $\sim$1 km s^{-1} less than usual at all crustal depths, which is interpreted in terms of transpression and brittle deformation acting on the fault zone [*van Avendonk et al.*, 2001]. Seismic studies reported that oceanic crust within large fracture zones consists of a thin, intensely fractured, and hydrothermally altered basaltic section overlying serpentinized mantle [e.g., *Detrick et al.*, 1993].

[32] The crustal thickness of $\sim$7.0 km found between profiles kms 0 and 170 may be expected for oceanic lithosphere formed at the fast Pacific-Farallon spreading center [*White et al.*, 1992; *Carbotte and Scheirer*, 2004]. Crustal thinning from 7.0 to $<$6.4 km in the trench coincides roughly with the intersection of the subducting Mocha FZ and the seismic line (Figure 2) and hence may suggest that thinner crust is related to the fracture zone. Some amount of this difference in crustal thickness may be attributed to uncertainties of the Moho depth (Figure 7d). However, as we described in section 5.2, Moho depth uncertainties are lower than 0.3 km in this part of the velocity-depth model. Therefore, a major part of thinning remains unexplained. Seismic measurements and rare Earth element inversions have evidenced crustal thinning beneath fracture zones [*White et al.*, 1992]. According to *Detrick et al.* [1993],
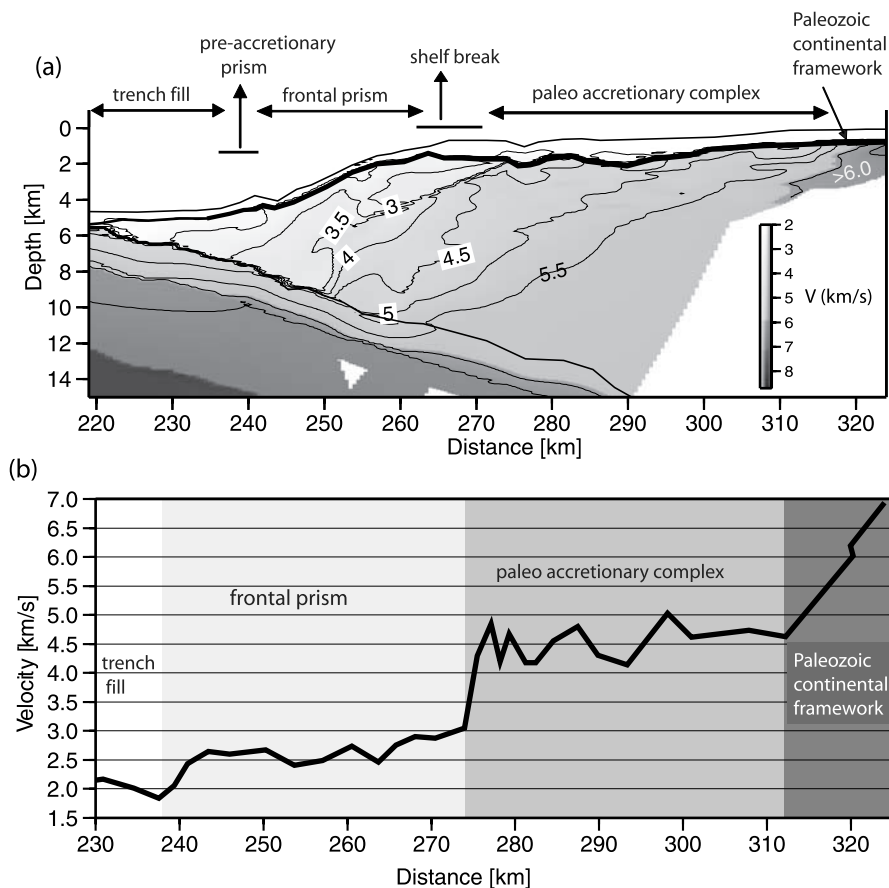
Figure 9. (a) Detailed tomographic image of the marine fore-arc complex, showing the seismic segmentation of the accretionary margin wedge. (b) Extracted velocities along the thick black line shown in Figure 9a, which landward of the lowermost slope corresponds to the uppermost basement velocities below the slope and shelf sediments. Note the strong horizontal velocity gradients at the slope break and seaward edge of the Paleozoic continental framework, which may suggest a change in rock type.

the thinning of the oceanic crust in fracture zones may be caused by a reduced magma supply within a broad region near ridge offsets due to the three-dimensional nature of upwelling beneath a segmented spreading center and by tectonic dismemberment of the crust by large-scale detachment faults that form preferentially in the cold, brittle lithosphere near the ends of segments.

[33] Oceanic fracture zones are characterized by a high degree of hydration in both the crust and mantle, and they commonly host bodies of serpentines deep into the oceanic lithosphere [*White et al.*, 1992]. The presence of the Mocha FZ may suggests a further potential source of fluids and provides an additional and natural explanation for the reduced low velocities in the crust and upper mantle. Furthermore, the projection of the Mocha FZ inland at the magmatic arc corresponds roughly with the location of the Longavi volcano, where the erupted magma composition has been studied [*Selles et al.*, 2004]. *Selles et al.* [2004] interpreted the magma composition to be high-degree mantle melts, highly hydrous and oxidized, formed as response to high fluid input into the subarc mantle. Thus, efficient water transport to the subarc mantle is a plausible effect of dehydration processes during the subduction of the Mocha FZ [*Selles et al.*, 2004].

6.2. Continental Margin

[34] Our interpretation of the margin structure is summarized in Figure 9. The seismic segmentation of the continental margin is defined by two high horizontal velocity gradients, one located at the shelf break and the other ~75 km from the deformation front. Figure 9b shows the lateral variation of the uppermost basement velocity within the marine fore arc (below the slope sediments and fore-arc basin). The horizontal velocity gradients define three main domains: (1) a wedged-shaped body of low velocity (<3.5 km s^{-1}) below the trench slope, which is interpreted as an active frontal prism, (2) a paleoaccretionary complex or metamorphic basement with Vp = 4.5– 5.5 km s^{-1}, and (3) the seaward edge of the Paleozoic continental framework (Vp > 6.0 km s^{-1}). The young frontal prism is approximately 20 km wide and hence in close agreement with previous seismic reflection results presented by *Bangs and Cande* [1997], *Diaz-Naveas* [1999] and *Grevemeyer et al.* [2003]. The most landward velocity transition zone coincides roughly with the onset of intraplate earthquakes located by *Haberland et al.* [2006], which are plotted in Figure 6b.

6.2.1. Seismic Segmentation of the Accretionary Margin

[35] Active frontal accretion processes at the seaward edge of the young accretionary wedge is evident by the style of deformation of the trench fill (Figure 4c). Here, sediment ridges represent a small fold-and-thrust belt caused by compressive sediment deformation (reverse faults). Reverse faults imaged within the trench basin control the current style of accretion. The transition from the upper slope to the continental shelf marks a gradual transition to stronger material, affecting the wedge stability and hence taper of the margin wedge [Davis et al., 1983]. The steep slope of the continental slope (~7°) offshore southern Arauco peninsula may indicate a transition from features formed during Miocene tectonic erosion [Encinas et al., 2008] to accretion at the present. Alternatively, the accretionary wedge may have thickened rapidly vertically during the Pliocene as a result of basal accretion beneath the prism and resulted in the steep slope. The accretionary prism is made up of trench sediments added to the toe of the margin, resulting in the seaward migration of the trench axis.

[36] The abrupt increase of seismic velocities roughly 60 km landward of the shelf break (at km 312) indicates a change of rock type (Figure 9) and might be associated with the seaward edge of the truncated Paleozoic continental framework [Mordojovich, 1974], whereas the inner wedge sandwiched between the frontal prism and this seismic "boundary" may correspond to a paleoaccretionary complex. Unfortunately, drilling did not sample crust from this geological unit but is confined to coastal sites, where basement rocks are of Paleozoic age [Mordojovich, 1974]. On the basis of the location of an exploratory well marked in Figure 2, the Paleozoic basement rock found here is located landward of the seaward edge of the continental framework (Figure 9a). Therefore, the composition and age of the proposed paleoaccretionary complex still remains unclear. It is interesting to note that the presence of a similar seismic "boundary" at roughly the same distance from the deformation front (70–80 km) has been observed farther to the south [Scherwath et al., 2007] and thus may form an integral part of the marine fore arc.

[37] The paleoaccretionary complex has a higher degree of consolidation and lithification than the frontal prism but lower than the Paleozoic continental framework. Alternatively, the unit interpreted as a paleoaccretionary complex might be part of the continental framework deformed and metamorphosed during a phase of tectonic erosion. However, the remarkable high lateral velocity gradient from 5.5 to >6.0 km s^{-1} favors a rapid change in rock type (Figure 9b), and hence alternation between accretion and erosional phases. The size of the paleoaccretionary complex should have been much larger at the end of the accretion phase, when the complex was formed. Thereafter, an integral part of the accretionary complex was tectonically eroded [Mordojovich, 1981; Melnick and Echtler, 2006; Encinas et al., 2008]. At present, the width of ~50 km of the paleoaccretionary complex represents the remaining material left after the last erosional phase, which took place in the Miocene according to Melnick and Echtler [2006] and Encinas et al. [2008]. Assuming alternation between accretion and erosion phases and based on the age of the oldest shelf sediments (Senonian age), we estimate that the paleoaccretionary complex might be formed of Jurassic age.

[38] The location of the seaward edge of the Paleozoic continental framework is well correlated with the onset of intraplate seismicity (Figure 6b) [Haberland et al., 2006], reflecting the interseismic transpressional deformation of the fore arc due to the subduction of the Nazca plate. In addition, this region coincides with the coastal uplifted area of the Arauco peninsula [Kaizuka et al., 1973] and belongs to the area of the Mocha block, which is characterized by high rates of modern seismicity [Habermann et al., 1986]. The interrelationship between intraplate seismicity and uplift of the Isla Mocha is complex, and may be associated to asperities on the plate interface beneath the Mocha block and the local structures within the upper plate [Kaizuka et al., 1973; Nelson and Manley, 1992]. Subduction of the Mocha FZ may explain the strength of the asperity beneath the Mocha block [Barrientos and Ward, 1990], which may induce upward stresses propagating through the overriding plate and activating crustal faults. Thus, intraplate seismicity in the upper and fragile part of the overriding plate could be induced, at least in part, by the subduction of the Mocha FZ.

6.2.2. Subduction of Sediments: The Subduction Channel

[39] Subduction of poorly consolidated sediments (subduction channel) beneath the overriding accretionary prism and crystalline block are usually assumed to be characterized by lower seismic velocities than the overriding structures, and thus may form a low-velocity zone (velocity inversion). However, this velocity contrast has not yet been constrained by seismic refraction experiments. A low-velocity layer cannot be resolved by the resolution of our refraction data, especially landward of the accretionary prism where the velocities are poorly constrained as is shown by the high-velocity uncertainties in Figures 7a and 7c. Our model, however, favors a more gradual velocity structure above the plate boundary and hence could not resolve a subduction channel.

[40] The existence of a decollement zone and hence subduction channel is usually derived from multichannel seismic reflection data (strong reflector, often with reversed polarity) or in ancient accretionary prisms in the form of tectonic mélanges and duplex structures [e.g., Kitamura et al., 2005]. Diaz-Naveas [1999] used depth-migrated MCS data to yield a ~1 km thick layer of subducting sediments above the top of the downgoing plate along profile ENAP-4 (Figure 1). The velocity contrast between the overlying prism and subducted sediments was rather small, roughly comparable with the velocity uncertainties of our tomographic model. Krawczyk and The SPOC Team [2003] and Groß et al. [2007] used near-vertical reflection data to image a region of high reflectivity with a thickness of 2–5 km above the plate boundary, which is located below the coast line at a depth of about 25 km at ~38.2°S. They interpret this reflectivity pattern as a subduction channel, which extends arcward for roughly 30 km [Groß et al., 2007]. However, in this case the thickness of the subduction channel would exceed the thickness of the trench fill and the thickness of the subduction channel imaged offshore [Diaz-Naveas, 1999; Bangs and Cande, 1997]. Therefore, the observed reflectivity pattern may represent laminated lower crust or shear zones within the continental crust, rather than a subduction channel.
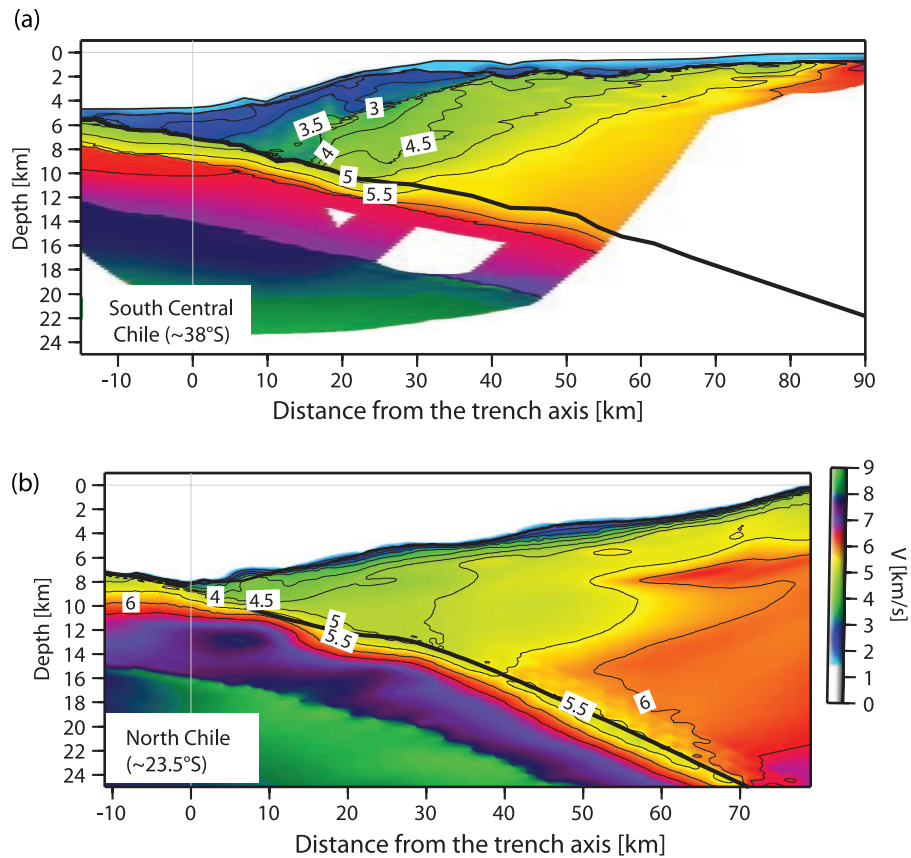
Figure 10. Direct comparison of the velocity depth models between (a) the young accretionary margin offshore of southern Arauco peninsula and (b) the northern erosional margin off Antofagasta [*Sallares and Ranero*, 2005].

6.2.3. Comparison With the Northern Erosional Chile Margin

[41] Figure 10 compares 2-D tomographic velocity models from the accretionary southern central and erosional northern Chile margin. *Sallares and Ranero* [2005] pointed out that the overriding plate in north Chile is mainly made of arc-type igneous basement, where the front of the margin is probably fluid-saturated, metamorphosed and disaggregated by fracturing as a consequence of frontal subduction erosion. The trench is sediment starved, the margin has no fore-arc basin, and the extensional regime across the continental slope has caused gravitational destabilization of the margin framework resulting in steepening of the margin related to progressive subduction erosion [*von Huene and Ranero*, 2003; *Ranero et al.*, 2006]. Offshore southern Arauco peninsula, in contrast, the trench is shallower and filled with up to 2.2 km of sediments, the continental shelf is broad (70–80 km), and has a well developed fore-arc basin. Uplift events and focal mechanism of intraplate events suggest that the margin suffers from compressional tectonics [*Kaizuka et al.*, 1973; *Barrientos and Ward*, 1990; *Haberland et al.*, 2006].

[42] A clear difference between these margins inferred from our tomographic model is the velocity structure at the front of the margin wedge. The frontal prism seaward of the shelf break off south central Chile has seismic velocities lower than 4 km s^{-1}, while off north Chile velocities are faster than 4 km s^{-1} (Figure 10). This observation indicates that the front of the southern central Chile margin is com-

posed of sediments, indicating accretionary processes. Off north Chile, in contrast, velocities >4 km s^{-1} are characteristic of igneous rocks rather than sedimentary rocks [*Sallares and Ranero*, 2005]. Velocities in the paleoaccretionary complex (landward of the shelf break) are >4 km s^{-1} (Figure 10a) and hence similar to the metamorphosed igneous continental crust off north Chile (Figure 10b). Metasedimentary and metamorphosed rocks are therefore indistinguishable in terms of seismic velocities. Nevertheless, the seismic tomography for the accretionary southern central Chile margin suggests a clear seismic segmentation, supporting episodes of accretion. In contrast, at the erosional northern Chilean margin, fracturing, alteration, and erosion have continuously lowered the velocity to the seaward edge of the margin, providing a gradual change of seismic velocity within the margin wedge.

7. Summary

[43] 1. Seaward from the area affected by bending-related faulting and the Mocha fracture zone (>120 km seaward of the trench axis), the oceanic crust is ~7 km thick and shows a typical P wave velocity structure generated during fast spreading. Here, uppermost mantle velocities are faster than ~8.4 km s^{-1}, suggesting an oceanic lithosphere that is relatively dry and undeformed.

[44] 2. Approaching the trench, seismic velocities decrease in both oceanic crust and mantle, indicating an evolutionary

process altering the structure of the lithosphere. This is likely related to an increase in fracture porosity and hydration of the oceanic lithosphere. In addition, extensional outer rise and horst-and-graben faults were mapped in the upper igneous crust and the seaward part of the trench fill sediment, defining the onset of bending-related faulting. Here, some extensional faults reach the seafloor, perhaps forming pathways for seawater into the underlying oceanic crust.

[45] 3. Reduced upper mantle velocities are confined to a region between the outer and inner trench wall with a maximum thickness of 6–8 km in the uppermost oceanic mantle and coincide with the isotherm of 400–430°C. This depth is interpreted as the lower limit for hydroalteration within the upper part of the oceanic lithosphere, where extensional stresses dominate.

[46] 4. The seismic profile crosses the subducting Mocha fracture zone at the trench. In this area inversion of P_mP arrivals support that crustal thickness is significantly reduced (10–15% thinning). Anomalous crust and mantle associated with the fracture zone may carry fluids and altered crustal and mantle rocks into the subduction zone.

[47] 5. A lateral seismic segmentation of the margin wedge was inferred from the tomographic model. Three main units are imaged: (1) a 15–20 km wide frontal accretionary prism below the continental slope with $Vp \leq 3.5$ km s^{-1}, (2) a ∼50 km wide block with $Vp = 4.5$–5.5 km s^{-1}, perhaps representing a paleoaccretionary complex or metamorphic basement, and (3) the truncated seaward edge of the Paleozoic continental framework with $Vp \geq 6.0$ km s^{-1}.

[48] 6. The seaward edge of the Paleozoic continental framework coincides with the onset of continental intraplate seismicity and the uplifted shelf offshore southern Arauco peninsula.

[49] 7. Frontal prism velocities are clearly lower than in the seaward section of the northern erosional Chile margin, where rocks are of metamorphosed igneous composition rather than sediments. Thus, the southern central accretionary Chile margin is characterized by a clear seismic segmentation, in contrast to the northern erosional margin, where seismic velocities gradually decrease toward the trench, interpreted to be linked to hydrofracturing and erosional processes [*von Huene and Ranero*, 2003; *Sallares and Ranero*, 2005].

References

Angermann, D., J. Klotz, and C. Reigber (1999), Space-geodetic estimation of the Nazca–South America Euler vector, *Earth Planet. Sci. Lett.*, 171(3), 329–334, doi:10.1016/S0012-821X(99)00173-9.

Bangs, N. L., and S. C. Cande (1997), Episodic development of a convergent margin inferred from structures and processes along the southern Chile margin, *Tectonics*, 16, 489–503, doi:10.1029/97TC00494.

Barrientos, S. E., and S. N. Ward (1990), The 1960 Chile earthquake: Inversion for slip distribution from surface deformation, *Geophys. J. Int.*, 103, 589–598, doi:10.1111/j.1365-246X.1990.tb05673.x.

Bialas, J., and E. R. Flueh (1999), Ocean bottom seismometers, *Sea Technol.*, 40(4), 41–46.

Carbotte, S. M., and D. S. Scheirer (2004), Variability of ocean crustal structure created along the global mid-ocean ridge, in *Hydrogeology of Oceanic Lithosphere*, edited by E. E. Davis and H. Elderfield, pp. 128–150, Cambridge Univ. Press, New York.

Carlson, R. L., and D. J. Miller (2004), Influence of pressure and mineralogy on seismic velocities in oceanic gabbros: Implications for the composition and state of the lower oceanic crust, *J. Geophys. Res.*, 109, B09205, doi:10.1029/2003JB002699.

Chapple, W. M., and D. W. Forsyth (1979), Earthquakes and bending plates at trenches, *J. Geophys. Res.*, 84, 6729–6749, doi:10.1029/JB084iB12p06729.

Christensen, N. I. (1996), Poisson's ratio and crustal seismology, *J. Geophys. Res.*, 101, 3139–3156, doi:10.1029/95JB03446.

Cifuentes, I. L. (1989), The 1960 Chilean earthquakes, *J. Geophys. Res.*, 94, 665–680, doi:10.1029/JB094iB01p00665.

Clift, P., and P. Vannucchi (2004), Controls on tectonic accretion versus erosion in subduction zones: Implications for the origin and recycling of the continental crust, *Rev. Geophys.*, 42, RG2001, doi:10.1029/2003RG000127.

Contreras-Reyes, E., I. Grevemeyer, E. R. Flueh, M. Scherwath, and M. Heesemann (2007), Alteration of the subducting oceanic lithosphere at the southern central Chile trench–outer rise, *Geochem. Geophys. Geosyst.*, 8, Q07003, doi:10.1029/2007GC001632.

Contreras-Reyes, E., I. Grevemeyer, E. R. Flueh, M. Scherwath, and J. Bialas (2008), Effect of trench-outer rise bending-related faulting on seismic Poisson's ratio and mantle anisotropy: A case study offshore of southern central Chile, *Geophys. J. Int.*, 173, 142–156, doi:10.1111/j.1365-246X.2008.03716.x.

Davis, D. M., J. Suppe, and F. A. Dahlen (1983), Mechanics of fold-and-thrust belts and accretionary wedges, *J. Geophys. Res.*, 88, 1153–1172, doi:10.1029/JB088iB02p01153.

Detrick, R. S., R. S. White, and G. M. Purdy (1993), Crustal structure of North Atlantic fracture zones, *Rev. Geophys.*, 31(4), 439–458.

Diaz-Naveas, J. L. (1999), Sediment subduction and accretion at the Chilean convergent margin between 35° and 40°S, Ph.D. thesis, Univ. of Kiel, Kiel, Germany.

Encinas, A., K. L. Finger, S. N. Nielsen, A. Lavenu, L. A. Buatois, D. E. Peterson, and J. P. Le Roux (2008), Rapid and major coastal subsidence during the late Miocene in south-central Chile, *J. South Am. Earth Sci.*, 25(2), 157–175, doi:10.1016/j.jsames.2007.07.001.

Flueh, E. R., and J. Bialas (1996), A digital, high data capacity ocean bottom recorder for seismic investigations, *Int. Underwater Syst. Design*, 18(3), 18–20.

Flueh, E. R., and I. Grevemeyer (Eds.) (2005), TIPTEQ SONNE Cruise SO-181, from the incoming plate to mega thrust earthquakes, *IFM-Geomar Rep. 102*, IFM-Geomar, Kiel, Germany.

Gonzalez, E. (1989), Hydrocarbon resources in the coastal zone of Chile, in *Geology of the Andes and Its Relation to Hydrocarbon and Mineral Resources*, edited by G. Ericksen et al., pp. 383–404, Circum-Pac. Counc. for Energy and Miner. Resour., Houston, Tex.

Grevemeyer, I., and W. Weigel (1996), Seismic velocities of the uppermost igneous crust versus age, *Geophys. J. Int.*, 124, 631–635, doi:10.1111/j.1365-246X.1996.tb07041.x.

Grevemeyer, I., N. Kaul, H. Villinger, and W. Weigel (1999), Hydrothermal activity and the evolution of the seismic properties of upper oceanic crust, *J. Geophys. Res.*, 104, 5069–5079, doi:10.1029/1998JB900096.

Grevemeyer, I., J. L. Diaz-Naveas, C. R. Ranero, H. Villinger, and Ocean Drilling Program Leg 202 Scientific Party (2003), Heat flow over the descending Nazca plate in central Chile, 32°S to 41°S: Observations from ODP Leg 202 and the occurrence of natural gas hydrates, *Earth Planet. Sci. Lett.*, 213, 285–298, doi:10.1016/S0012-821X(03)00303-0.

Grevemeyer, I., N. Kaul, J. L. Diaz-Naveas, H. Villinger, C. R. Ranero, and C. Reichert (2005), Heat flow and bending-related faulting at subduction trenches: Case studies offshore of Nicaragua and central Chile, *Earth Planet. Sci. Lett.*, 236, 238–248, doi:10.1016/j.epsl.2005.04.048.

Grevemeyer, I., C. R. Ranero, E. R. Flueh, D. Klaeschen, and J. Bialas (2007), Passive and active seismological study of bending-related faulting and mantle serpentinization at the Middle America trench, *Earth Planet. Sci. Lett.*, doi:10.1016/j.epsl.2007.04.013.

Groß, K., U. Micksch, and the TIPTEQ Research Group, Seismic Team (2007), The reflection survey of project TIPTEQ—The inventory of the Chilean subduction zone at 38.2°S, *Geophys. J. Int.*, 172, 565–571, doi:10.1111/j.1365-246X.2007.03680.

Haberland, C., A. Rietbrock, D. Lange, K. Bataille, and S. Hofmann (2006), Interaction between forearc and oceanic plate at the south-central

Chilean margin as seen in local seismic data, *Geophys. Res. Lett.*, *33*, L23302, doi:10.1029/2006GL028189.

Habermann, R. E., W. R. McCann, and B. Perin (1986), Spatial seismicity variations along convergent plate boundaries, *Geophys. J. R. Astron. Soc.*, *85*, 43–68, doi:10.1111/j.1365-246X.1986.tb05171.x.

Herron, E. M., S. C. Cande, and B. R. Hall (1981), An active spreading center collides with a subduction zone, a geophysical survey of the Chile margin triple junction, *Mem. Geol. Soc. Am.*, *154*, 683–701.

Herve, F. E., F. Munizaga, M. A. Parada, M. Brook, R. Pankhurst, N. Spelling, and R. Drake (1988), Ganitoids of the coast range of central Chile: Geochronology and geologic setting, *J. South Am. Earth Sci.*, *1*(2), 185–194, doi:10.1016/0895-9811(88)90036-3.

Ivandic, M., I. Grevemeyer, A. Berhorst, E. R. Flueh, and K. McIntosh (2008), Impact of bending related faulting on the seismic properties of the incoming oceanic plate offshore of Nicaragua, *J. Geophys. Res.*, *113*, B05410, doi:10.1029/2007JB005291.

Kaizuka, S., T. Matsuda, M. Nogami, and N. Yonekura (1973), Quaternary tectonic and recent seismic crustal movements in the Arauco Peninsula and its environs, central Chile, *Geogr. Rep. 8*, pp. 1–49, Tokyo Metrop. Univ., Tokyo.

Kitamura, Y., et al. (2005), Mélange and its seismogenic roof décollement: A plate boundary fault rock in the subduction zone—An example from the Shimanto Belt, Japan, *Tectonics*, *24*, TC5012, doi:10.1029/2004TC001635.

Kopp, H., E. R. Flueh, C. Papenberg, and D. Klaeschen (2004), Seismic investigations of the O'Higgins Seamount Group and Juan Fernández Ridge: Aseismic ridge emplacement and lithosphere hydration, *Tectonics*, *23*, TC2009, doi:10.1029/2003TC001590.

Korenaga, J., W. S. Holbrook, G. M. Kent, P. B. Kelemen, R. S. Detrick, H.-C. Larsen, J. R. Hopper, and T. Dahl-Jensen (2000), Crustal structure of the southeast Greenland margin from joint refraction and reflection seismic tomography, *J. Geophys. Res.*, *105*, 21,591–21,614, doi:10.1029/2000JB900188.

Krawczyk, C., and The SPOC Team (2003), Amphibious seismic survey images plate interface at 1960 Chile earthquake, *Eos Trans. AGU*, *84*(32), 301.

Krawczyk, C. M., et al. (2006), Geophysical signatures and active tectonics at the south-central Chilean margin, in *Frontiers in Earth Sciences: The Andes—Active Subduction Orogeny*, edited by O. Oncken et al., pp. 171–192, Springer, Berlin.

Lefeldt, M., and I. Grevemeyer (2008), Centroid depth and mechanism of trench-outer rise earthquakes, *Geophys. J. Int.*, *172*, 240–251.

Masson, D. G. (1991), Fault patterns at outer trench walls, *Mar. Geophys. Res.*, *13*, 209–225, doi:10.1007/BF00369150.

Melnick, D., and H. Echtler (2006), Inversion of forearc basins in south-central Chile caused by rapid glacial age trench fill, *Geology*, *34*(9), 709–712, doi:10.1130/G22440.1.

Mikumo, T., Y. Yagi, S. K. Singh, and M. A. Santoyo (2002), Coseismic and postseismic stress changes in a subducting plate: Possible stress interactions between large interplate thrust and intraplate normal-faulting earthquakes, *J. Geophys. Res.*, *107*(B1), 2023, doi:10.1029/2001JB000446.

Mordojovich, C. (1974), Geology of a part of the Pacific margin of Chile, in *The Geology of Continental Margins*, edited by C. A. Burk and C. L. Drake, pp. 591–598, Springer, New York.

Mordojovich, C. (1981), Sedimentary basins of the Chilean Pacific offshore, *AAPG Stud. Geol.*, *12*, 732–749.

Müller, R. D., W. R. Roest, J.-Y. Royer, L. M. Gahagan, and J. G. Sclater (1997), Digital isochrons of the world's ocean floor, *J. Geophys. Res.*, *102*, 3211–3214, doi:10.1029/96JB01781.

Nelson, A. R., and W. F. Manley (1992), Holocene coseismic and aseismic uplift of Isla Mocha, south-central Chile, *Quat. Int.*, *15–16*, 61–76, doi:10.1016/1040-6182(92)90036-2.

Ranero, C. R., and V. Sallares (2004), Geophysical evidence for alteration of the crust and mantle of the Nazca Plate during bending at the north Chile trench, *Geology*, *32*, 549–552, doi:10.1130/G20379.1.

Ranero, C. R., J. Phipps Morgan, K. McIntosh, and C. Reichert (2003), Bending, faulting, and mantle serpentinization at the Middle America Trench, *Nature*, *425*, 367–373, doi:10.1038/nature01961.

Ranero, C. R., A. VillaseÃtor, J. Phipps Morgan, and W. Weinrebe (2005), Relationship between bend-faulting at trenches and intermediate-depth seismicity, *Geochem. Geophys. Geosyst.*, *6*, Q12002, doi:10.1029/2005GC000997.

Ranero, C. R., R. von Huene, W. Weinrebe, and C. Reichert (2006), Tectonic processes along the Chile convergent margin, in *Frontiers in Earth*

Sciences: The Andes—Active Subduction Orogeny, edited by O. Oncken et al., pp. 91–121, Springer, Berlin.

Reichert, C., B. Schreckenberger, and the SPOC Team (2002), Fahrtbericht SONNE-Fahrt SO-161 Leg 2&3 SPOC, Subduktionsprozesse vor chile-BMBF-Forschungsvorhaben 03G0161A-Valparaiso 16.10.2001-Valparaiso 29.11.2001, Bundesanst. für Geowis. und Rohstoffe, Hannover, Germany.

Sallares, V., and C. R. Ranero (2005), Structure and tectonics of the erosional convergent margin off Antofagasta, north Chile (23°30′S), *J. Geophys. Res.*, *110*, B06101, doi:10.1029/2004JB003418.

Scherwath, M., E. Flueh, I. Grevemeyer, F. Tilmann, E. Contreras-Reyes, and W. Weinrebe (2006), Investigating subduction zone processes in Chile, *Eos Trans. AGU*, *87*(27), 265, doi:10.1029/2006EO270001.

Scherwath, M., E. Contreras-Reyes, I. Grevemeyer, E. R. Flueh, W. Weinrebe, and TIPTEQ Research Group (2007), Upper lithosphere structure of the subduction zone in southern Chile: Comparison of differently aged incoming plate, *Geophys. Res.*, *Abstr.*, *9*, S.06798.

Selles, D., A. C. Rodríguez, M. A. Dungan, J. A. Naranjo, and M. Gardeweg (2004), Geochemestry of Nevado de Longavi Volcano (36.2°S): A compositionally atypical arc volcano in the southern volcanic zone of the Andes, *Rev. Geol. Chile*, *31*(2), 293–315.

Seno, T., and Y. Yamanaka (1996), Double seismic zones, compressional deep trench-outer rise events and superplumes, in *Subduction: Top to Bottom*, *Geophys. Monogr. Ser.*, vol. 96, edited by G. Bebout et al., pp. 347–355. AGU, Washington, D. C.

Tarantola, A. (1987), *Inverse Problem Theory: Methods for Data Fitting and Model Parameter Estimation*, 613 pp. Elsevier, New York.

Tebbens, S. F., S. C. Cande, L. Kovacs, J. C. Parra, J. L. LaBrecque, and H. Vergara (1997), The Chile ridge: A tectonic framework, *J. Geophys. Res.*, *102*, 12,035–12,060, doi:10.1029/96JB02581.

Thornburg, T. M., and D. M. Kulm (1987), Sedimentation in the Chile Trench: Depositional morphologies, lithofacies, and stratigraphy, *Geol. Soc. Am. Bull.*, *98*, 33–52, doi:10.1130/0016-7606(1987)98<33:SITCTD>2.0.CO;2.

Thornburg, T. M., D. M. Kulm, and D. M. Hussong (1990), Submarine-fan development in the southern Chile trench: A dynamic interplay of tectonics and sedimentation, *Geol. Soc. Am. Bull.*, *102*, 1658–1680, doi:10.1130/0016-7606(1990)102<1658:SFDITS>2.3.CO;2.

Tilmann, F. J., I. Grevemeyer, E. R. Flueh, T. Dahm, and J. Goßler (2008), Seismicity in the outer rise offshore southern Chile: Indication of fluid effects in crust and mantle, *Earth Planet. Sci. Lett.*, *269*, 41–55, doi:10.1016/j.epsl.2008.01.044.

Turcotte, D., and G. Schubert (1982), *Geodynamics-Applications of Continuum Physics to Geological Problems*, 464 pp., John Wiley, Hoboken, N. J.

Vallée, M., M. Bouchon, and S. Y. Schwartz (2003), The 13 January 2001 El Salvador earthquake: A multidata analysis, *J. Geophys. Res.*, *108*(B4), 2203, doi:10.1029/2002JB001922.

van Avendonk, H. J. A., A. J. Harding, and J. A. Orcutt (1998), A two-dimensional tomographic study of the Clipperton transform fault, *J. Geophys. Res.*, *103*, 17,885–17,899, doi:10.1029/98JB00904.

van Avendonk, H. J. A., A. J. Harding, J. A. Orcutt, and J. S. McClain (2001), Contrast in crustal structure across the Clipperton transform fault from travel time tomography, *J. Geophys. Res.*, *106*, 10,961–10,982, doi:10.1029/2000JB900459.

Voelker, D., M. Wiedicke, S. Ladage, C. Gaedicke, C. Reichert, K. Rauch, W. Kramer, and C. Heubeck (2006), Latitudinal variation in sedimentary processes in the Peru-Chile trench off central Chile, in *Frontiers in Earth Sciences: The Andes—Active Subduction Orogeny*, edited by O. Oncken et al., pp. 193–216, Springer, Berlin.

von Huene, R., and C. R. Ranero (2003), Subduction erosion and basal friction along the sediment-starved convergent margin off Antofagasta, Chile, *J. Geophys. Res.*, *108*(B2), 2079, doi:10.1029/2001JB001569.

White, R. S., D. McKenzie, and R. K. O'Nions (1992), Oceanic crustal thickness from seismic measurements and rare Earth element inversions, *J. Geophys. Res.*, *97*, 19,683–19,715, doi:10.1029/92JB01749.

E. Contreras-Reyes, E. R. Flueh, and I. Grevemeyer, Leibniz-Institute of Marine Sciences, University of Kiel, Wischhofstrasse 1-3, D-24148 Kiel, Germany. (econtreras-reyes@ifm-geomar.de)

C. Reichert, Federal Institute for Geosciences and Natural Resources, Stilleweg 2, D-30655 Hannover, Germany.